Geochemical signatures of mid-crustal melting processes and heat production in a hot orogen: the Kerala Khondalite Belt, Southern India

Accepted Manuscript

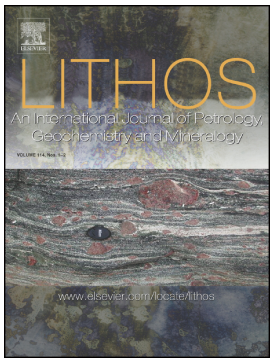

Geochemical signatures of mid-crustal melting processes and heat production in a hot orogen: The Kerala Khondalite Belt, Southern India

V. Nandakumar, Simon L. Harley

PII: S0024-4937(18)30431-6
DOI: https://doi.org/10.1016/j.lithos.2018.11.016
Reference: LITHOS 4870

To appear in: *LITHOS*

Received date: 3 August 2018
Accepted date: 15 November 2018

Please cite this article as: V. Nandakumar, Simon L. Harley , Geochemical signatures of mid-crustal melting processes and heat production in a hot orogen: The Kerala Khondalite Belt, Southern India. Lithos (2018), https://doi.org/10.1016/j.lithos.2018.11.016

Geochemical signatures of mid-crustal melting processes and heat production in a hot orogen: the Kerala Khondalite Belt, Southern India

V. Nandakumar[1], Simon L. Harley[2,*]

[1]ESSO-National Centre for Earth Science Studies, Ministry of Earth Sciences, Government of India, Thiruvananthapuram, Kerala, India - 695 031.

v.nandakumar66@gmail.com

[2] School of Geosciences, University of Edinburgh, James Hutton Road, Edinburgh, UK, EH9 3FE.

simon.harley@ed.ac.uk*

*Corresponding author

Abstract

Garnet-bearing migmatites and associated leucogranites and leucosomes of the Trivandrum Block in the Kerala Khondalite Belt were formed through granulite facies dehydration melting of metasedimentary protoliths. Significant trace element depletions in Cs, Zr, Nb and the compatible transition metal elements V, Cr, Ni, Cu and Zn relative to average post-Archaean shales and model middle and upper crust, recorded in all samples, require their sedimentary protoliths to have been impure sandstones and greywackes, rather than shales. Leucogranites (70-75wt %) and leucosomes (SiO_2: 68-70wt %), which are uniformly peraluminous and classed as S-type on the basis of their A/NK and ASI relations, form a compositional array that shows strong correlated variations between TiO_2 and Fe_2O_3, and TiO_2 or Fe_2O_3 with Co and Y. These reflect coupled variations in modal garnet and ilmenite and require the presence of up to 15-20 wt% of entrained peritectic garnet in the higher Y and HREE leucosomes. The leucosomes have REE patterns with normalised La/Sm of 10, negative Eu anomalies (Eu* < 0.8) and flat HREE at 6-20 times chrondrite, whereas leucogranites range to much lower HREE (1-5 times chondrite) with higher La/Sm and large positive Eu anomalies (Eu* = 1.4-3.4). Despite broadly similar major element compositions that lie within the granite minimum melt field in terms of felsic components, leucogranite Zr contents are highly variable, ranging down to 4-20 ppm in the lowest HREE and high Eu* cases, resulting in Zr saturation temperatures (544-647ºC) that are lower than any feasible melt. These geochemical features, coupled with covariations between Nb,-Ta and Y-Yb, collectively support petrological and field observations that the leucosomes are mixtures between former melt and entrained peritectic garnet and ilmenite. The leucogranites are the products of melt extraction and migration on metres to several metres lengthscales. Leucogranite Nb-Y, Ta-Yb, Eu* and Sr-Ba relationships demonstrate that their chemical

diversity is principally controlled by variation in peritectic phase assemblage, i.e. proportion of entrained garnet, ilmenite and K-feldspar, with near-situ feldspar-dominated fractional crystallisation and accumulation coupled with the loss of fractionated melt being secondary controls. Age-corrected heat productions of the best-segregated leucogranites that most closely approach melt compositions are 2.7±0.8 μWm^{-3}, somewhat greater than the weighted average, 1.7 ± 0.5 μWm^{-3}, of preserved migmatite, in-situ leucosomes and leucogranites of all types. Correction of the 550 Ma heat production to account for an estimated 30% of migration and loss of melt from this middle crustal migmatite complex yields a syn-orogenic heat production of c. 2.0 ± 0.6 μWm^{-3} which, though elevated compared with model middle-crust, is unlikely to have been high enough to have facilitated the near-UHT to UHT metamorphism in the Trivandrum Block without the addition of heat external to the orogenic crust itself.

Keywords: Migmatite, leucogranite, geochemistry, heat production, Kerala Khondalite Belt

1. Introduction

The mineralogical, textural, isotopic and geochemical characteristics of migmatitic granulites provide important evidence for evaluating the processes involved in crustal differentiation and granite genesis in collisional zones and accreted continental arcs (Vielzeuf et al., 1990; Brown 1994, 2004). Whilst H_2O-saturated melting in the deep crust is possible in some circumstances, it is inevitable that under medium-pressure granulite P-T conditions of 5-10 kbar and >850ºC the predominant partial melting reactions are incongruent (peritectic) dehydration-melting reactions that progress through the breakdown of hydrous minerals (e.g. Thompson, 1982; Clemens and Vielzeuf, 1987; Waters, 1988) and give rise to water-undersaturated melts and largely anhydrous residues. This concept has been supported experimentally for a range of pelite and semipelite rock compositions (Vielzeuf and Holloway, 1988; Patiño-Douce and Johnston, 1991; Skjerlie and Johnston, 1993; Koester et al., 2002) and more recently by an extensive body of calculated phase equilibria modelling founded upon such experimental studies (e.g. Johnson et al., 2008; Yakymchuk et al., 2017).

In the simplest sense, it is envisaged that the widespread presence of felsic granitic melts at upper crustal levels should be complemented by bodies of anhydrous melt-depleted granulites deep in the continental crust (Vielzeuf et al., 1990). According to Brown (1994) and Sawyer (1998) partial melting can play a key role in initiating geochemical differentiation during crustal reworking. Deformation during orogenesis will allow transient and evolving networks of flow paths to facilitate melt extraction and ascent (Brown and Rushmer, 1997; Weinberg and Searle, 1998; Brown and Solar, 1998; Vanderhaeghe, 2009; Yakmchuk et al., 2013). Hence, deeply eroded orogens are important sites to study the relevant melting processes and the scales of melt

transfer associated with the formation of crustally-derived granites (Brown, 2004, 2013; Brown and Solar, 1998; Sawyer, 1994, 2001; White and Powell, 2002).

The Kerala Khondalite Belt (KKB), southern India, is comprised of granulite-facies rocks formed during the assembly of eastern Gondwana (e.g. Braun et al., 1998; Collins et al., 2007, 2014; Santosh et al., 2005, 2009). The KKB contains abundant migmatitic gneisses and leucogranites that have been the subject of several studies focussed on melting reactions and local-scale melt retention and loss (e.g. Cenki et al., 2002; Braun and Bröcker, 2004; Kriegsmann, 2001; Harley and Nandakumar, 2014), and the preservation of melt compositions in the form of nanogranites (Cesare et al., 2009), but to date no comprehensive study of the broader geochemical signatures of migmatisation and melt distribution in the KKB has been undertaken. Here we present the geochemistry of migmatites, leucosomes and leucogranites, and residual (restitic) rocks from the Trivandrum Block of the KKB and consider this with respect to the scales over which near-source processes control the chemical signatures of the melts extracted from this large-scale mid-crustal migmatite complex and the implications for the distribution of heat-producing elements. The textural and compositional variety of migmatites in the Trivandrum Block and their fresh exposure in active quarries offer an excellent opportunity to examine the role of melting, melt migration and retention or loss during high grade metamorphism, processes that also influence the rheological behaviour of the crust during collisional orogeny (Jamieson and Beaumont, 2013).

2. Geological Setting and Previous studies

The Trivandrum Block (Fig. 1; Santosh, 1996) forms the north-eastern part of the Kerala Khondalite Belt of southern India. It is an elongate, NW-SE trending gneiss complex that is bounded to its NE by the Achankovil Shear Zone, and to the SW by the Nagercoil Block.

The Trivandrum Block is comprised dominantly of migmatitic garnet-biotite-quartz-feldspar gneisses and garnet-cordierite-sillimanite gneisses (khondalites), as well as granitic orthogneisses, charnockites and localised mafic granulites. Zircon in granitic and charnockitic orthogneisses suggest magmatic protolith ages of 2.1-2.0 Ga, 1.88-1.84 Ga and 1.76 Ga (Kröner et al., 2012, 2015; Whitehouse et al., 2014). Migmatitic garnet-biotite-quartz-feldspar gneisses and khondalites record Archaean (3.3-2.7 Ga) to Palaeoproterozoic (2.0 Ga) Nd model ages (Bartlett et al., 1998; Cenki et al., 2004; Harris et al., 1994), consistent with 2.7-1.9 Ga $^{207}Pb/^{206}Pb$ age spectra obtained from detrital zircon cores (Collins et al., 2007). At Kanjampara quarry (KNJ; Fig. 1) Harley and Nandakumar (2016) documented a relict > 1.9 Ga high grade metamorphic event involving anatexis and melt segregation, proving that at least some of the metasediments in the Trivandrum Block are polymetamorphic and therefore may have experienced migmatisation and melt loss prior to Neoproterozoic to Cambrian tectonism.

The dominant regional granulite-facies metamorphism and migmatisation in the Trivandrum Block is latest Neoproterozoic to Cambrian in age. Metamorphic ages defined from near-concordant zircon rims in orthogneisses, migmatitic leucosomes and paragneisses lie in the range 570-515 Ma (e.g. Braun and Bröcker, 2004; Cenki et al., 2004; Collins et al., 2007; Collins et al., 2014; Clark et al., 2015; Harley and Nandakumar, 2014; Kröner et al., 2012, 2015; Santosh et al., 2005, 2009; Shabeer et al., 2005; Taylor et al., 2014; Whitehouse et al., 2014). U-Pb ages of anatectic zircons and monazites in migmatite leucosomes (Taylor et al., 2014; Harley and Nandakumar, 2014) indicates cooling of the Trivandrum Block granulites to an elevated residual granite solidus by 523 ± 7 Ma.

Pressure and temperature (*P–T*) estimates for the Neoproterozoic-Cambrian metamorphism in the Trivandrum Block range from early estimates of 5.5–7.0 kbar at 700–800°C (Chacko et al,

1997) to 925 ± 20°C at 6.5–7.0 kbar (Nandakumar and Harley, 2000; Braun and Bröcker, 2004). Based on pseudosection analysis Cenki et al. (2002) obtained a clockwise P–T path culminating at 6–7 kbar and 900–950°C, consistent with that defined by Nandakumar and Harley (2000). Although Morimoto et al. (2004) and Tadokoro et al. (2008) suggested UHT conditions of greater than 950°C, at pressures up to 12 kbar, the most recent estimates based on calculated phase diagrams have confirmed peak metamorphic conditions in the range 830-925°C and 6-9 kbar followed by suprasolidus decompression (Blereau et al, 2016).

3. Field Relations and Petrography

Detailed field studies were undertaken in the following eleven localities (working quarries) from south to north across the Trivandrum Block (Fig. 1): Kulappara (KLP), Pallikkal (PLK), Kanjampara (KNJ), Kannimala (KNN), Kairali (KAI), Nellikkala (NEL), Asarimala (ASM), Kottapara (KTP), Malakkara (MLK), Cherukol (CKL), and Kurambala (KBL) (Supplementary Table S1).

All quarries are characterised by garnet-bearing migmatitic gneisses, either cordierite-bearing or lacking in cordierite, and associated leucosomes that occur as 1-10 centimetre pockets and patches and as decimetre to several decimetre width layer-parallel veins or sheets (Fig. 2). The latter structures anastomose and coalesce along their length on scales of a few decimetres to several metres (Fig. 2a, 2c, 2g). Leucosomes have portions that are comprised of >95% quartz + feldspar with minor garnet and/or cordierite (Fig. 2b, 2c), in some cases interspersed with schlieren rich in cordierite, garnet and/or sillimanite (Fig. 2d). Coarse subhedral porphyroblastic garnet, occasionally pseudomorphed by cordierite, occurs within leucosomes, both as isolated grains (Fig. 2c, 2g) but also spatially associated with the schlieren (Fig. 2d, 2h). Graphite may be present as millimetre-sized flakes within leucosomes and on leucosome margins, which may also

be rich in biotite, cordierite and ilmenite. Residual or 'restitic' gneisses are rich in garnet, ilmenite and/or magnetite, cordierite, plagioclase and sillimanite, and generally lack quartz and K-feldspar.

Discordant leucogranitic veins may also occur, cutting the migmatitic gneisses, associated leucosomes and near-concordant leucogranites on metre to several metre scales (Fig. 2e, 2h). An example of this type of vein from Kulaparra (KLP, Fig. 1) has been documented in detail by Harley and Nandakumar (2014).

4. Petrology

Thirty three thin sections were prepared at the National Centre for Earth Science Studies (NCESS) thin section facility. Twenty-eight polished thin sections were prepared in the lapidary facility of the University of Edinburgh for accessory mineral phase identification, SEM and CL imaging, EPMA and SIMS analysis.

The main gneissic rock types are dominated by foliated layers alternating with less abundant granular leucocratic layers or lenses, and hence are collectively classified and hereafter referred to as migmatites. These migmatites are garnet-cordierite-sillimanite-ilmenite bearing pelitic to semipelitic gneiss and minor orthopyroxene-bearing garnet-cordierite-ilmenite-(magnetite)-spinel aluminous gneiss (e.g. Nellikala – NEL, Fig. 1). The most common assemblage comprises Grt + Crd + Sill + Bt + Kfs + Qtz + Pl + Fe-Ti oxides ± green spinel (generally associated with the ilmenite and magnetite) with accessory zircon, monazite and apatite. The migmatites are characterised by alternating 5 millimetre to 1 centimetre width garnet-cordierite-sillimanite (+ Fe-Ti oxides) and garnet-bearing quartzo-feldspathic leucosome layers. Orthopyroxene-bearing garnet-cordierite gneiss that occur at Nellikala (NEL) and Kairali (KAI, Fig. 1) quarries are characterized by bluish patches comprised by cordierite aggregates (Fig. 2b), set in a typical

assemblage of coarse-grained garnet (2–4 mm) and orthopyroxene (3–4 mm), with quartz, plagioclase, spinel, biotite, K-feldspar (perthite), ilmenite, magnetite and cordierite.

Leucosomes and leucogranites are dominated by quartz, K-feldspar (mainly perthitic) and plagioclase, with minor (<5 modal %) garnet, lobate ilmenite and clusters of sillimanite needles. Overall textures range from hypidiomorphic and oikocrystic in leucogranites to lobate and sutured granoblastic with significant grain-boundary recrystallisation in some leucosomes. Garnet is usually poikiloblastic, containing rounded inclusions of quartz and subhedral inclusions of zircon and monazite, but also may be xenomorphic, forming a sieve-like intergrowth with optically continuous quartz on 1-5 millimetre grain scales.

5. Geochemistry

5.1. Analytical Methods

Major and selected trace elements were determined by XRF at the National Centre for Earth Science Studies (NCESS), Trivandrum, using a Bruker S4 Pioneer sequential wavelength-dispersive x-ray spectrometer equipped with a 7-crystal goniometer (OVO-55, PET, LiF 200, LiF 220, Ge, ADP and InSb), 4 kW Rh X-ray tube, 0.23 and 0.46° collimators and supported by SPECTRA plus software for determination of elemental abundances. Fifteen standards were used to define calibration curves for analysis (G2, GSP2, STM1, SARM1, SARM2, SY3, RGM, GA, GH, GS-N, AC-E, MDOG, ISHG, VS-N, JG-1+, JG-2+, JG-3+, JR-3+, JSY-1+). Additional trace element and REE whole rock analyses were obtained at the National Geophysical Research Institute (NGRI), Hyderabad, India, using a Perkin Elmer ICPMS - Elan DRC II instrument and three granite standards (USGS standards G-1 and G-2; Japanese standard granite JG-2). Major element analyses and calculated molecular norms are presented in Table 1, trace element analyses and relevant trace element ratios in Table 2, and REE analyses and chondrite-

normalised REE data in Table 3. A compilation of all the geochemical data is provided in Appendix A2.

5.2. Major Element Compositions and Variations

The SiO_2 contents of the samples range from 57 to 75 wt%. Combined with the field relations and petrographic features noted in a previous section, this supports the classification of the rocks into four groups: 'restite' or residual gneisses (SiO_2=57-60 wt%), migmatites (SiO_2=60-66 wt%), leucosomes (SiO_2=68-70 wt%) and leucogranites (>70wt% SiO_2). The distinction between leucosome and leucogranite is somewhat arbitrary as it is based on sampling scale relative to size of the leucocratic vein or layer. Where the whole leucocratic vein or layer was sampled, up to its adjacent walls, the sample is denoted as 'leucosome'. Where the geochemical sample was smaller than the width of the leucocratic vein or sheet and taken from the centre of that sheet the sample is denoted as 'leucogranite'.

Major elements correlate strongly, either positively or negatively, with SiO_2 and are consistent between rock types (Fig. 3). The lower SiO_2 restites have amongst the highest CaO and Na_2O, reflecting plagioclase contents similar to and higher than the migmatites, but as a consequence do not have the highest total Fe_2O_3 + MgO + TiO_2. Leucogranites, with >70% SiO_2, have the lowest TiO_2, Fe_2O_3 + MgO and CaO, highest K_2O, and Na_2O that overlaps with migmatites. The relationship between TiO_2 and SiO_2 is representative of most FM components also – TiO_2 decreases with increasing SiO_2, as do Fe_2O_3 and MgO. Leucogranites anchor this trend at high SiO_2, and migmatites follow it to lower SiO_2 but with more scatter. The petrographic features noted above indicate that this scatter is caused by both biotite and ilmenite contributing to the TiO_2 budget in migmatites, whereas in the leucogranites ilmenite is the principal or sole TiO_2 phase.

Bulk compositions of all of the rock types are presented in terms of normative proportions of felsic components in figure 4a and 4b. Leucosomes and leucogranites plot within the field of granites in terms of both the wt% normative Qz-Ab-Or (Fig. 4a) and Qz-Plag-Or (Fig 4b) ternary projections, clustering close to and to the Qz-Or side of experimentally-determined ternary minimum melt compositions in the haplogranitic system (Johannes and Holtz, 1996). The leucogranites and leucosomes are peraluminous, with ASI near or above 1.1 and A/NK>1.3 (Fig. 5a), and straddle the ferroan:magnesisan granitoid boundary of Frost et al. (2001). Based on these criteria they can be identified as 'S-type' in character, although they are not equivalent to S-type granites *sensu stricto* (Stevens et al., 2007; Nicoli et al., 2017) as they generally lack biotite and show only minor variations in Na_2O and K_2O relative to CaO (Fig. 3). Migmatites plot within or close to the 'granite' field when projected into the Qz-Ab-Or ternary (Fig. 4a), but range to high normative Ab+An (Plag) and hence lie outside the granite field in Qz-Plag-Or pseudoternary space (Fig. 4b). Restites, and one migmatite, have low wt% normative Qz relative to the other rock types.

The bulk compositions have been recast in terms of K_2O-FeO-MgO-Al_2O_3-SiO_2 (KFMAS) components after correction for Na and Ca (attributed to plagioclase, and also apatite in the case of Ca) and Ti (attributed to ilmenite) and plotted on the AFM projection of Figure 4c. The projected positions of 850-950°C experimental melts produced by Skjerlie et al. (1993) and Koester et al. (2002) are also shown, as well as the positions of garnet (Grt), cordierite (Crd) and biotite (Bt) solid solutions with representative limiting compositions (in X_{Mg}) as determined from mineral analyses of representative samples (e.g. Nandakumar and Harley, 2000; Harley and Nandakumar, 2014). Leucogranites form a linear array between garnet and sillimanite, lying on or near a garnet control line and ranging up to the experimental melts in most cases. The

anomalously high A/AFM leucogranites KNJ1 and KNJ3 are from the Kamjampara locality where Harley and Nandakumar (2016) identified a Palaeoproterozoic anatectic episode. The four leucosomes straddle the garnet compositional line, reflecting the presence of garnet as the principal Fe-Mg phase. Most migmatites lie within the three-phase field Grt + Crd + Bt/Opx (+ Plag + Ilm + Kfs + Qz), consistent with their observed mineralogy. A small number are more aluminous, and plot within or near the Grt + Crd + Sil field accordingly. Restites, or residual, gneisses are more magnesian (similar to the migmatites), with Grt + Bt/Opx or Grt + Bt/Opx + Crd forming the principal ferromagnesian phase assemblages.

5.3 Trace Element Compositions and Variations

The transition metals and HFSE trace element variations between samples and rock types can be evaluated by plots of selected elements against Fe_2O_3 or TiO_2 (Fig. 6).

TiO_2 and Fe_2O_3 correlate strongly for all samples, implying control on these by shared mineral phases. However, the main data trend defines a Fe_2O_3 / TiO_2 slope of 6:1 that is well above the vector for ilmenite control, which is 1:1 in wt% terms. The slope is also too high to reflect biotite control (Fe_2O_3 / TiO_2 slope 2.9-3.6 based on Nandakumar and Harley (2000); Fig. 6a), and petrographic observation of a lack of biotite in those leucogranite samples with <4 wt% Fe_2O_3 further points to the correlation being controlled by garnet together with ilmenite. In this case, 1 wt% TiO_2 equates to 2 wt% ilmenite, and the amount of garnet required to account for the remaining Fe_2O_3 in the highest Fe_2O_3-TiO_2 sample in the leucogranite-leucosome suites is ca. 15 wt%.

Cr is similar between all samples and rock types, showing no variation with TiO_2 or Fe_2O_3. V, Co and Ni all increase with TiO_2 at TiO_2 contents less than 0.4 wt%, but show more scatter at higher TiO_2 and hence Fe_2O_3. Positive correlations of Co and V with both TiO_2 (Fig. 6) and

Fe_2O_3 in the leucogranites is consistent with ilmenite control on the trace element variations. In contrast, V and Co show weak or no positive correlation with TiO_2 in the four leucosomes. This is consistent with garnet contributing to the higher Fe_2O_3, and biotite to the higher TiO_2 and Fe_2O_3, in these rocks.

Ni and Zn (Fig. 6), and Cu, show only weak correlations with TiO_2. These trace elements tend to follow the same trends as Fe_2O_3 versus TiO_2, with Ni and Zn being highest in the highest Fe_2O_3 migmatite (Fig. 7). This indicates that principal mineralogical controls on these trace elements at high Fe_2O_3 contents are either sulphides or magnetite, or a combination of these phases. Overall, the large variations in Ni, Zn and Cu in the Trivandrum Block migmatites reflect variable modal proportions of ilmenite, magnetite, pyrite and chalcopyrite. Of these, ilmenite is by far the dominant opaque and pyrite is the most common sulphide.

Nb (and Ta) correlates closely with TiO_2, particularly in the leucogranites and leucosomes (Fig. 6), consistent with ilmenite control on these trace elements. Extrapolation of the Nb versus TiO_2 correlation observed for leucogranites up to TiO_2 wt% characteristic of ilmenite indicates that the constituent ilmenites contain ~ 1000-1200 ppm Nb.

Sr and Rb display opposite trends with respect to SiO_2, with leucogranites and leucosomes having higher Rb and lower Sr contents than migmatites and residual rocks (Fig. 8). Rb essentially follows K_2O, and hence normative Or contents (Fig. 8a, 8b), whereas Sr correlates strongly with CaO and moderately with Na_2O, reflecting plagioclase control (Fig. 8c, 8d).

Trace element abundance patterns for the Trivandrum Block samples are presented normalised against average middle continental crust of Rudnick and Gao (2003) in Figure 9. Migmatites and restites have abundances of the elements from Ga to Ba that are lower than or close to average middle continental crust, with the exception of Cs, which is highly depleted relative to middle

continental crust and post Archaean average shales (PAAS, Fig. 9c). The transition metals, apart from Co, are also markedly depleted in the migmatites and restites in comparison to average middle continental crust. Middle-crust normalised leucosome and leucogranite trace element patterns show many similar features to those of the migmatites (Fig. 9), but as noted through consideration of the variations described above (Fig. 6, 7, 8) are depleted in V, Co, Ni and Sr, and enriched in Rb, relative to migmatites and restites. The high Rb/Cs (530 ± 280) and marked depletions in Cs, V, Cr, Ni and Cu (and to a lesser extent Zr) relative to middle continental crust appear to be primary chemical attributes of the Trivandrum Block gneisses as these features are shared by all the rock types analysed. This issue is considered further in the discussion (section 6.1).

5.4 REE Patterns and Variations

Chondrite-normalised REE patterns are presented in Figure 10. Leucogranites can be divided into two varieties: those with negative Eu anomalies (Eu* < 1), similar to leucosomes, and those with positive or negligible Eu anomalies (Eu* > 1). The leucosomes and leucogranites with negative Eu anomalies have high LREE, from La(n) of 100-600 to Sm(n) at 30-100, and somewhat fractionated MREE-HREE with Gd(n)/Yb(n) in the range 3-10. The normalised MREE-HREE span over an order of magnitude, for example from 30 to 5 for Dy(n) and 20 to 2 for Yb(n). Leucogranite-leucosome MREE-HREE, and Y, contents correlate strongly with bulk-rock Fe_2O_3 (Fig. 11).

Leucogranites with positive Eu anomalies have low LREE (La(n) = 20-50; Sm(n) = 5-10) compared with the group noted above. Four of these leucogranites have low and flat MREE-HREE at 2-6 times chondrite. The fifth example, KNJ-3, has the lowest LREE and very low HREE at < 1 times chondrite. This sample has the highest normative felsic components

(An+Ab+Or+Qz = 95% of the norm) and lowest normative FM components (1 mol% Ilm + Opx; A/AFM = 78; Fig. 4c) of any of the leucogranites in this study. The presence of sillimanite trails in the analysed volume leads to c. 3.8 mol% normative corundum being calculated in this highly feldspathic sample.

Migmatites to some extent overlap the leucogranites that have negative Eu* but may range to higher HREE (Fig. 10c). Only a few of the migmatites have HREE contents that approach or exceed PAAS; several lie at only 2-10 times chondrite (Fig. 10c). The MREE-HREE that correlate with Fe_2O_3 in leucogranites and leucosomes plateau in all but the most Fe-rich migmatite (Fig. 11). Five of the studied migmatites and three restites preserve distinctly low Y and Dy contents at elevated Fe_2O_3 (Fig. 11), well below the compositional trend consistent with garnet control. This is considered to reflect the presence of biotite and/or other low-HREE Fe-Mg minerals (e.g. orthopyroxene, cordierite) in these samples.

5.5 Zr Concentrations and Zirconium Saturation Temperatures

Zr concentration data for all the Trivandrum Block rocks are presented in Figure 12a. All samples apart from two leucosomes (MLK-1, MLK-2) and one leucogranite (KBL-3) contain <130 ppm Zr. Migmatite and restite Zr contents largely overlap those of the leucogranites, which range down to the lowest Zr contents measured (3 samples with < 10 ppm Zr). The Zr contents of leucogranites and leucosomes are considered in relation to other chemical indices for these rocks in Figure 12b and 12c. Zr saturation temperatures (Table 4) calculated using the solubility thermometer of Watson and Harrison (1983) are annotated on these diagrams. Zr contents plotted against total Nb+Y as an index of ilmenite plus garnet content (Fig. 12b) show that all samples with Nb+Y less than 40 ppm have Zr<90 ppm, equating to apparent zirconium saturation temperatures from 544°C to 762°C. Only those samples with higher Nb+Y, and hence high

ilmenite + garnet modes, have higher Zr contents that yield saturation temperatures of 790-830°C. Zr contents plotted against the Eu anomalies of the leucogranite or leucosome (Fig. 12c) demonstrates that the four leucogranites with the lowest Zr contents (<30 ppm Zr) are characterised by strongly positive Eu anomalies (Eu* > 1). The apparent zirconium saturation temperatures (544-647°C) obtained for these samples are lower than feasible melting temperatures at the documented pressures of metamorphism (6-7 kbar: Nandakumar and Harley, 2000). Leucogranite KNJ-3, which has the lowest Zr contents (4 ppm) and hence zirconium saturation temperature, also has severe deletions in Y, Nb and Ta, the lowest HREE of any analysed sample, and anomalously high A/AFM. This sample, and the other leucogranite samples with Zr < 30 ppm, cannot represent melt compositions but rather are more likely to reflect feldspar (+quartz) crystals accumulated during the passage of melt. If this is the case, the extremely low, and varied, Zr contents in these leucogranites could reflect the retention of small volumes of interstitial melt in the feldspathic cumulate. This is considered further in the discussion.

5.6 Th, U and K Concentrations and Heat Production Estimates

Th, U and K_2O concentrations have been converted into estimated present day and 550 Ma heat productions (Table 5) using the equation of Clauser (2011), and with concentrations at 550 Ma age-corrected using the relevant decay constants. 550 Ma has been chosen to approximate the age of the final HT-UHT metamorphism and melting in the Trivandrum Block. The calculated heat productions, which use densities computed from the wt% normative mineralogies of the rocks, were on average 10% higher at 550 Ma than present day values. These 550 Ma heat production estimates are shown in figure 13, plotted for all samples against total Th+U concentration (Fig. 13a) and for leucogranites and leucosomes against Nb+Y (Fig. 13b)

Migmatite 550 Ma heat productions range from very low (0.45 μWm^{-3}) up to just over 2 μWm^{-3} and average at 1.2 ± 0.5 μWm^{-3}, which is similar to the median of 1.16 +0.62/-0.48 μWm^{-3}. None of these migmatites have total Th+U contents greater than 20 ppm (average 7.4 ppm Th, 1 ppm U). The heat productions of the migmatites at a given Th+U content are lower than leucogranites and leucosomes (Fig. 13a) because of the lower average K contents of the migmatites (2.9 wt% vs 5.2 wt% K_2O).

Leucosomes and leucogranites collectively yield an average 550 Ma heat production of 2.38 ± 1.25 μWm^{-3}. The median heat production, 2.38 +1.28/-1.57 μWm^{-3}, in this case reflects skew in the data caused by inclusion of the leucosomes, which have distinctively high TiO_2, Nb and Y (Fig. 13b). Considering the leucogranites alone, total heat productions correlate with TiO_2, ranging from 0.5-1.0 μWm^{-3} for the lowest-TiO_2 samples and up to 3.4 μWm^{-3} in the case of leucogranites with c. 0.4 wt% TiO_2. The calculated average 550 Ma heat production for all the leucogranites, 2.0 ± 1.1 μWm^{-3}, is considered further in the discussion section following analysis of the potential roles of peritectic assemblage entrainment, melt loss, and crystal fractionation in producing the range in their trace element chemistries. Leucosomes yield the highest average heat productions, 3.7 ± 1.0 μWm^{-3}, but as only four have been analysed this average should not be taken without due caution as representative of leucosomes within the Trivandrum Block in general.

6. Discussion

6.1 Protoliths of the Trivandrum Block Migmatites

The trace element compositions of the Trivandrum Block migmatites and related rock types have been compared with continental middle crust in section 5.3 and Figure 9. As upper continental crust lies to higher values of these trace elements than model middle crust (Rudnick and Gao,

2003), the Trivandrum Block rocks are clearly strongly depleted in Cs, V, Cr, Ni, Cu and Zr relative to model upper continental crust. This observation prompts the question of what protolith best matches the trace element patterns that are preserved in the Trivandrum Block rocks despite the extensive anatexis evident in the granulites. Comparison of the migmatites with post-Archaean Australian shale (PAAS), greywacke, and sandstone averages compiled by McLennan (2001) indicates that their trace element chemistry is more compatible with a greywacke or mixed sandstone/siltstone protolith than with shale (Fig. 9c), although the possibility that the preserved trace element depletions, particularly of Cs and U, have arisen through the variable re-melting of previously melt-depleted gneisses (e.g. Melo et al., 2017) may also be considered, given that samples from Kanjampara (KNJ) preserve incontrovertible evidence for a separate anatectic event at 1.9 Ga.

The potential role of earlier melting in generating the elemental depletions is evaluated by comparing the relative depletions of Cs and U, both of which would be partitioned strongly into melt, relative to the incompatible elements Rb and Th. In this comparison the averaged concentration of each element in the migmatite samples is referenced against its abundance in average continental upper and middle crust based on the compilations of Rudnick and Gao (2003) and the relative depletions between the elements calculated. Cs is depleted relative to both Th and Rb by a factor of 12 ± 2 when referenced against middle crustal values for each element, and by 20 ± 2 when referenced against the upper crustal abundances. The same analysis shows that Cs is strongly depleted, by a factor of 9 ± 1, relative to U for both middle and upper crust reference values. Hence, although U (and Zr) in the migmatites is relatively depleted, Cs is significantly more depleted in comparison to other incompatible elements that would be lost through earlier melt extraction. As a consequence, the marked Cs signature that is shared by all

the Trivandrum Block samples cannot be explained simply by the re-melting of rocks that had already lost melt in an earlier (e.g. Palaeoproterozoic) melting episode. Whilst earlier melting of some gneisses cannot be ruled out, and indeed may be the case for leucogranites KNJ1 and KNJ3 from Kanjampara that exhibit relative depletions in U that are of similar magnitude to Cs (e.g. Cs depleted by a factor of 1.5-2.5 relative to U), the global depletion in Cs is more likely to have been inherited from the sedimentary protoliths. On the basis of their low Cs and transition metal contents relative to shales and middle or upper crust it is concluded that impure arenites and immature greywackes or siltstones are appropriate protoliths for the Trivandrum Block migmatites.

6.2 Major elements, leucogranite compositions and melt-related processes

Bulk composition data for all the rock types are plotted in Figure 14 in terms of the molar percentages of the 'felsic' components K and Na+Ca, and the 'ferromag' components Fe+Mg+Ti, following Solar and Brown (2001). This representation is complementary to those presented in Figure 4, as quartz is in excess and variations in Al_2SiO_5 or the 'A' component are not depicted. Melts produced under granulite facies conditions in three representative experimental studies of natural rocks are shown as coloured elliptical fields, with corresponding starting material compositions depicted as stars. The studies of Patiño-Douce and Harris (1998) and Koester et al. (2002) used pelite starting materials, whilst that of Skjerlie et al. (1993) used a greywacke composition. Leucogranites in the present study plot in the broad area defined by the experimental melts, whereas four leucosomes plot to higher mol % Fe+Mg+Ti, trending towards the compositional field occupied by the migmatites. The trend to higher Fe+Mg+Ti in the leucosomes reflects higher garnet (and/or cordierite and ilmenite) contents relative to feldspars.

Collectively the major element correlation diagrams and molar or component projections indicate that much of the compositional variation in the leucogranites and leucosomes is controlled by garnet, ilmenite and K-feldspar and/or plagioclase. For example, the leucogranite-leucosome array on the AFM diagram (Fig. 4c) could be interpreted to reflect either fractionation, entrainment, or a lack of separation of peritectic or wall-rock garnet. Given the lack of biotite in most, if not all, leucogranites in this study, the leucogranite compositions that are more magnesian than the garnet control line reflect the presence of orthopyroxene or cordierite as the main Fe-Mg peritectic phases in those samples.

On the basis of major elements alone it is apparent that whilst the leucogranites approach minimum melt compositions (Fig. 4a), in detail they deviate from those in being either residual, representing accumulations of feldspar (the low Fe+Mg+Ti leucogranites), or in containing additional crystals of ilmenite and garnet that drive the bulk compositions towards higher projected A/AFM (Fig. 4c) and Fe+Mg+Ti (Fig. 14) Leucosomes continue the latter trend but also lie between the leucogranites and migmatites and to the high-Na+Ca side of the garnet-leucogranite join on Figure 14. This may reflect the presence of additional plagioclase in the leucosomes, either entrained from wall rock migmatite during passage of the melt or simply through incorporation of adjacent host rock in the geochemical analysis.

This type of compositional diversity in leucogranites and leucosomes has been described extensively from other migmatite terrains, and a number of processes or mechanisms have been invoked to explain it (e.g. Sawyer, 2001; Solar and Brown, 2001; Stevens et al, 2007; Taylor and Stevens, 2010; Clemens, 2012; Brown, 2013; Morfin et al., 2014; Yakymchuk et al., 2015; Carvahlo et al, 2017; Garcia-Arias and Stevens, 2017). These include melt fractionation, restite unmixing, peritectic phase assemblage entrainment, wall- or host-rock mineral entrainment, and

combinations of these. The dominant processes cannot be clarified using major elements alone, but can be assessed in some cases using diagnostic trace element and REE criteria. The mechanisms responsible for the composition variations in the Trivandrum Block leucogranites and leucosomes are further evaluated here using the trace element and REE data presented above.

6.3 Trace element and REE constraints on leucogranite geochemical variations: the roles of crystal accumulation and peritectic assemblage entrainment

Trace element discriminant diagrams (TEDDs) using combinations of Rb (incompatible), Nb, Ta (HFSE), Y and a representative HREE such as Yb (Pearce et al., 1984) are presented in Figure 15. Whilst the higher-Y and -Yb leucogranites and leucosomes overlap with the migmatites in their Nb and Ta contents, the latter have significantly lower Rb and range to considerably higher Y+Nb and Ta+Yb contents and hence can be distinguished on that basis.

In detail the leucogranites and leucosomes form linear arrays with correlations between Y and Nb, and Ta and Yb. Rb is shows little variation across all Y, Nb and Ta+Yb contents. Such data, if assumed to represent trace element concentrations in melts, could be interpreted in terms of a number of tectonic associations on the basis of the positions of the analyses on the trace element diagrams (Figure 15). However, as demonstrated from the orogenic geological setting of the leucogranites and leucosomes in the Trivandrum Block as well as the preceding analysis of trace element correlations with TiO_2 and Fe_2O_3, the observed trends in the HFSE and HREE elements do not reflect any real variation in sourcing or tectonic setting but instead result from the mixed nature of the rocks, which may include former melts with entrained or accumulated phases or melts that have undergone near-situ crystal fractionation, or combinations of these.

The leucogranites that lie towards the Na+Ca side of the Solar and Brown (2001) diagram (Fig. 14) have very low Nb (< 4ppm), Yb (<0.9 ppm) and Y (<11 ppm), and lie to the lower ends of the TEDD arrays of Figure 15. They also have strong positive Eu* anomalies, and generally low Zr contents (four are <21 ppm; one at 62 ppm) that equate to zirconium saturation temperatures in the range 544-647°C and 728°C. As noted in a previous section the lower temperature range is unfeasible for any granitic liquid. These geochemical features collectively support the interpretation that these leucogranites represent accumulations of early-formed crystals of feldspar in melts that have been extracted through the leucosome / leucogranite network and hence mostly removed from the local chemical environment (Sawyer, 2001; Solar and Brown, 2001; Brown, 2004, 2013; Morfin et al., 2014). Leucogranite KNJ-3, with 95% normative QAP components and only 3 mol% Fe+Mg+Ti, has the lowest Zr, Nb, Ta, Y and Yb contents of any of the samples, a strong positive Eu* and highly depleted HREE, all consistent with it being essentially a quartz-feldspar cumulate. The other four examples of positive Eu* leucogranites have higher Y and Yb contents and flat HREE indicating the presence of minor garnet, and variable Nb and Ta contents reflecting the presence of negligible to minor ilmenite. The low LREE (La(n) = 20-50) of these leucogranites confirms their broadly cumulate character, in which case the higher HREE and variable Nb+Ta might result from the capture of minor amounts of peritectic garnet and ilmenite in the cumulate framework, potentially along with small volumes of interstitial melt. The amount of melt potentially retained in the four leucosomes of strongly cumulate character, which have 4-21 ppm Zr, can be estimated by simple mass balance assuming that all the Zr resides in the trapped melt and given an estimate for the saturation Zr content of that melt. For assumed crystallisation temperatures of 790-850C the saturation Zr contents are 150-200 ppm (e.g. Figure 12c). Hence, if the cumulate plus retained melt model is applicable,

KNJ-3 (4 ppm Zr) would have retained 2-3 wt% melt, KNJ-1 (21 ppm Zr) 10-12 wt% melt, and the other two leucosomes 4-6 wt% melt. Such low melt fractions are reasonable in that they are similar to or lower than the melt percolation threshold often applied in modelling of melt extraction from migmatites (Brown, 2013). The 550 Ma heat productions associated with these cumulate leucogranites is 0.9±0.3 μWm^{-3}.

The leucogranites that best approximate the experimental melts (Fig. 4c, 14), and hence may represent melts that have not undergone extensive phase entrainment, or appreciable feldspar accumulation coupled with melt loss, are characterised by 72.8 wt% SiO_2, peraluminous with A/NK of 1.44 and ASI of 1.22, and ferroan with FeO(t)/F+M of 0.83. In terms of the more compatible trace elements these contain ca. 6.5 ppm Nb and 0.3 ppm Ta, 13±8 ppm Y and 0.8 ppm Yb. They have variable Rb (120-395 ppm), Sr (80-214 ppm) and Ba (310-1150 ppm), with Sr and Ba broadly correlated. Their Zr contents are 67±18 ppm, yielding apparent Zr saturation temperatures of 724±27°C (Table 4; Watson and Harrison, 1983). These potential melt compositions plot in the syn-COLG field when Rb is considered along with Y, Yb, Nb and Ta (Fig. 15a, 15b). The 550 Ma heat productions at associated with these leucogranites is 2.8±0.6 μWm^{-3}.

The samples with the highest Ta+Nb and Y+Yb include the garnet-bearing leucosomes, which also have elevated TiO_2 as shown by the bivariate plots of figure 6, and hence elevated ilmenite contents. As noted previously, the Fe_2O_3-TiO_2 correlation with a wt% slope of 6:1 (Fig. 6) implies that increasing modes of garnet and ilmenite are correlated for the higher Fe+Mg+Ti leucogranites and leucosomes, corresponding to 14 wt% garnet and 2 wt% ilmenite (i.e. garnet:ilmenite 7:1 wt% ratio, which is equivalent to a 2.3:1 molar ratio).

The roles of garnet and ilmenite are explored and refined further in Figure 15 using the measured Y and Yb contents of typical Trivandrum Block garnets as determined by Harley and Nandakumar (2014) coupled with Nb and Ta contents of ilmenites extrapolated from the TiO_2 correlations in figure 6. These mixing calculations are therefore independent of any assumptions regarding the behaviour or mineralogical siting of Fe_2O_3. This is illustrated, for example, by the positions of garnet and ilmenite on the Nb-Y diagram and the vectors associated with addition of these phases to a melt.

The calculations show that the Nb-Y and Ta-Yb arrays can be generated by the incorporation of up to 22 wt% of garnet and ilmenite in the phase proportions of 9 wt% ilmenite and 91 wt% garnet, a 3.5:1 molar garnet:ilmenite ratio . If the leucogranites that approximate experimental melt compositions are regarded as melts then their Nb-Y and Ta-Yb compositions lie at ca. 7 wt% total garnet and ilmenite, in the same garnet:ilmenite ratio. Hence, by difference the higher Y and Yb leucogranites and leucosomes would represent melt plus between zero and 15 wt% of garnet and ilmenite, of which ilmenite would constitute 1.2 wt% and garnet 13.8 wt%. These trace element modelling results are within error of those obtained using the Fe_2O_3-TiO_2 correlation, and confirm that the spread of leucogranite to leucosome compositions largely can be generated by the incorporation of garnet and ilmenite in constant proportions. As shown by Stevens et al. (2007), Villaros et al. (2009) and Taylor and Stevens (2010), and modelled in depth by Garcia-Arias and Stevens (2017), the addition of phases in near-constant proportions is a key feature of peritectic assemblage entrainment. In this scenario crystals of two or more phases produced along with melt as a result of a dehydration-melting reactions may be left at sites of melt extraction to then be available to be entrained into further melts as those melts migrate along conduits and effectively sweep up the grains on conduit walls or in crystal-rich

pockets (e.g. Brown, 2013). As the solid phase and melt proportions are dictated by the melting reactions the peritectic minerals will be left behind in those proportions at sites of melt extraction and potentially entrained in the same proportions, unless one of the minerals preferentially adheres to conduit walls.

Modelling of the dehydration melting of pelites and greywackes for the proportions of phases produced with melt on clockwise prograde heating paths at mid-crustal pressures (6-8 kbar) (Yakymchuk et al., 2017) indicates that peritectic garnet and ilmenite are indeed produced over the temperature range from c. 700° to 900°C. The proportion of peritectic garnet increases relative to ilmenite throughout the temperature interval over which biotite reacts out, to reach near-constant garnet:ilmenite proportions at T>850°C. For the model pelite and greywacke considered by Yakymchuk et al. (2017) the molar proportions of garnet to ilmenite at T>850°C are 8:1 and 9:1 respectively. This would reflect the maximum proportion of garnet in the peritectic assemblage, achieved when biotite is exhausted from the melting assemblage and when melt constitutes some 35-40 mol% of the model pelite or 15-20 mol% of the model greywacke.

Whilst illustrating the constant peritectic phase ratio concept, the proportion of garnet relative to ilmenite in the partial melting of these model compositions is significantly higher than in the Trivandrum Block migmatites (model molar ratios 8-9:1 vs calculated 2.3-3.5:1). This important difference arises not from any process of preferential density settling, but from the differences between the model rocks and likely bulk compositions of the sedimentary precursors to the Trivandrum Block migmatites. Whilst these are not known directly, as demonstrated here from consideration of their trace element systematics (Fig. 9), the Trivandrum Block migmatite percursors were lower in their transition metal contents, and hence also in TiO_2, than typical pelites and greywackes. Theriak-Domino (de Capitani and Petrakakis, 2010) phase equilibrium

modelling of partial melting of the average migmatite of this study at 850-900°C and 7 kbar yields garnet and ilmenite as peritectic phases in the molar ratio 3.7:1, forming some 28 wt% of the solid phase assemblage coexisting with leucogranitic melt. In this case some 25-28 wt% melt, or 32 volume% melt, is produced at 850-900°C, the generally accepted temperature range for regional metamorphism and partial melting in the Trivandrum Block (Harley and Nandakumar, 2014; Clark et al., 2015). The very good agreement between the garnet:ilmenite ratio obtained from the Theriak-Domino phase equilibrium modelling and that derived from both the Fe_2O_3-TiO_2 major element correlation and Nb-Ta-REE mixing model approaches supports the interpretation that peritectic assemblage entrainment plays a central role in producing the geochemical variation observed in the Trivandrum block leucogranites and leucosomes, with the latter representing melt, or melt plus peritectic or early crystallised feldspar, along with up to 15 wt% of peritectic garnet plus ilmenite.

Given that K-feldspar is also produced as a peritectic phase in the biotite-controlled melting reaction producing the Trivandrum Block migmatites and leucogranites (e.g. Harley and Nandakumar, 2014) it might be expected that this phase will also be entrained to a similar extent as the garnet and ilmenite, leading to geochemical variability. This, along with the role of feldspar crystal fractionation from near-situ melts, is considered in the following section.

6.4 Sr-Ba constraints on leucogranite geochemical variations: the roles of near-situ feldspar crystal fractionation and accumulation

As described in the preceding sections, whilst some of the Trivandrum Block leucogranites may approximate melts, overall they range from those that are cumulate in character, with low HREE and positive Eu* typical of feldspar accumulation, to potentially fractionated compositions with REE patterns typical of highly evolved melts and with low Sr and Ba contents. The roles played

by K-feldspar, and to a lesser extent plagioclase, in generating the compositional variability in the leucogranites and leucosomes can be assessed through consideration of their Sr-Ba systematics.

Morfin et al. (2014) considered the role of feldspar-dominated crystal fractionation on leucogranite chemistry in the Archaean Opinaca Subprovince of northern Québec. They explained their observed spectrum of Sr-Ba compositions (Fig. 16a), which spanned an order of magnitude in Sr and nearly two orders of magnitude in Ba, as the result of extensive near-situ crystal fractionation of early-crystallised alkali and plagioclase feldspar along with quartz and minor biotite and garnet.

Figure 16a shows the Sr-Ba compositions of the Trivandrum Block leucogranites and leucosomes. Most lie at lower Sr, for a given Ba content, than the Opinaca leucogranites of Morfin et al. (2014), and though the range in Sr is about an order of magnitude, the range in Ba for all except one sample (PLK-2) is an order of magnitude less than in the Opinaca case. The Trivandrum Block leusosomes and leucogranites that most closely approximate experimental melts and exhibit Nb-Ta-Y-Yb evidence for peritectic phase assemblage entrainment form a cluster at >500 ppm Ba that shows limited covariation of Sr with Ba. Four leucogranites with Ba less than 300 ppm define a steep Sr-Ba trend to very low Sr (21 ppm, PLK-2).

The impact of feldspar crystal fractionation on the Sr-Ba systematics has been modelled for an arbitrarily assumed starting liquid composition containing 100 ppm Sr and 500 ppm Ba that lies adjacent to the Sr-Ba field defined by both leucogranites and leucosomes. (grey diamond on Fig. 16a). The modelling has been carried out or three crystallising phase assemblages: 100% K-feldspar, 70% K-feldspar - 30% plagioclase, and 50% Kfeldspar – 50% plagioclase, using the same distribution coefficients for Sr and Ba as applied by Morfin et al. (2014). These result in

the model melt fractionation lines, contoured for % feldspar fractionated (diamond-shaped symbols on each curve), that track down to the low Sr-Ba corner of the diagram. The Sr-Ba trend for the four lower-Ba leucogranites (short dashed line) is closest in slope to the model crystal fractionation trend for the fractionation of Kfeldspar and plagioclase in 50:50 wt% proportions and consistent with up to 30% fractionation of these minerals to produce the lowest-Sr leucogranite; the total percentage of fractionation will be greater with quartz also present as a fractionating phase.

The relationships between Ba, and hence Sr, and HFSE element character of the leucogranites and leucosomes is shown in Figure 16b. The four low-Ba leucogranites that lie on the Sr-Ba trend indicative of extensive feldspar fractionation in Figure 16a have intermediate Nb+Y contents. This is compatible with a negligible peritectic garnet and ilmenite entrainment in these particular leucogranites. The remaining higher-Ba leucogranites range from those with elevated Nb+Y approaching and overlapping that of the leucosomes, reflective of peritectic phase assemblage entrainment (Fig. 16b), to three with Nb+Y less than 10 ppm, potentially indicative of feldspar accumulation with melt loss.

The effect of feldspar accumulation on the Sr-Ba geochemistry of the leucogranites and leucosomes is also illustrated in figure 16a. Two calculated mixing curves are presented, one for the accumulation of K-feldspar alone (black circled symbols at 5 wt% K-feldspar intervals) and the other for the accumulation of Kfeldspar and plagioclase in equal wt% amounts (purple filled circled symbols up to 20 wt% total feldspar accumulated / entrained). Leucosomes follow the K-feldspar alone trend, with up to 5-8 wt% K-feldspar accumulated, depending on the starting melt composition used. As K-feldspar is formed as a peritectic phase along with garnet and ilmenite this result is consistent with peritectic phase assemblage entrainment. The higher-Ba

leucogranites show a spread in Sr and Ba and hence do not follow the K-feldspar alone trend. Instead, the Sr-Ba features of these leucogranites can be explained by the accumulation of both K-feldspar and plagioclase, up to perhaps 20 wt% in total. This is complementary to the inference of crystal fractionation having affected the low Sr-Ba leucogranites, albeit with initial variations in Ba being implied by the offset between the two geochemical trends.

In summary, the evidence from the variations in HFSE and HREE elements coupled with those observed in Rb, Sr and Ba in the leucogranites and leucosomes, considered in concert with initial constraints from their major element features, strongly indicates that peritectic phase assemblage entrainment, limited feldspar-controlled crystal fractionation and the complementary accumulation of early-formed near liquidus feldspars have all contributed to the geochemical diversity recorded in these rocks. All of these processes are operating at or near source, so that the melts that must have escaped from the crustal section represented by the Trivandrum Block in order to allow the preservation of high-temperature and relatively anhydrous mineral assemblages (Kriegsman, 2001; White and Powell, 2002) are likely to include not only weakly- or little-fractionated types (higher Ba and Sr) but also, to some extent, more fractionated and evolved melts. The nature of the melts that have left the crustal section will have consequences for the residual heat production of the remaining, somewhat melt-depleted, migmatite terrain. This is considered briefly in the following section.

6.5 Orogenic Heat Production in the Trivandrum Block

Based on the data presented in Table 5 and Figure 13, coupled with the grouping of leucogranites defined above from trace element geochemistry, the 550 Ma heat productions at associated with the leucogranites that most closely approximate experimental melts is 2.7±0.8 μWm^{-3}. That associated with the cumulate leucogranites is 0.9±0.3 μWm^{-3}, and that for the fractionated low

Sr-Ba leucogranites 1.4±0.9 μWm^{-3}. Based on the migmatite and leucosome data (Table 5) the 550 Ma heat production of the khondalites of the Trivandrum Block, calculated assuming retention of 7% leucosome in the migmatites and neglecting the contribution of retained leucogranite is 1.4 ± 0.5 μWm^{-3}. If the average higher Sr-Ba leucogranite heat production of 2.7 μWm^{-3} is representative of melts that have been extracted from the crust now exposed in the Trivandrum Block, then assuming the production of some 20% leucogranite the average heat production at 550 Ma of the crust at the present erosion level of the Trivandrum Block is calculated to have been 1.7 ± 0.6 μWm^{-3}. An upper limit on this would assume extraction of 30% of the highest heat production leucogranite (2.7 μWm^{-3}), in which case the reintegrated middle crustal heat production at 550 Ma would be 2.0 ± 0.6 μWm^{-3}. Coupling these results with estimates of the pressures of metamorphism of 6-7 kbar obtained from the granulites (Chacko et al, 1997; Nandakumar and Harley, 2000; Braun and Bröcker, 2004) and correcting for densities suggests that this component of the middle to deep orogenic crust at 20-25 km depths had syn-metamorphic heat productions similar to or greater than those of modern day model upper crust (1.58 μWm^{-3}: Rudnick and Gao, 2003) and considerably higher than model middle crust (0.34-0.72 μWm^{-3}: Rudnick and Gao, 2003). This type of migmatitic gneiss constitutes some 50% of the exposed Trivandrum Block (Figure 1), and is complemented mainly by garnet-biotite gneisses that are unlikely to have significantly higher heat productions. If this is the case, the heat production of the orogenic middle- to deeper-crust of the Trivandrum Block, though elevated, would only be about 50-60% of that required for radiogenic self-heating of that crust alone to produce the near-UHT to UHT conditions attained in the orogen at 550-520 Ma (ca. 3.5 μWm^{-3} in an initial crustal layer 20 km thick: Clark et al., 2011). The relatively long-lived near-UHT to UHT metamorphism of the Trivandrum Block (Clark et al., 2015; Harley, 2016; Blereau

et al., 2016) would, on the basis of these calculations, require the addition of significant heat from sources external to the orogenic crust itself in order to undergo its extensive melting and attain the high temperatures recorded in its granulites.

7. Conclusions

1. The source rocks for the Trivandrum Block migmatitic gneisses were semipelitic sediments characterised by REE patterns and Ga, Rb, Nb, Ta, Y and Ba contents that are lower than or similar to post-Archaean shales and average model middle crust, and by significant relative depletions in the transition metals (Sc, V, Cr, Ni, Cu and Zn), Zr and Cs that bear strong similarities to average arenites.

2. Leucogranites and leucosomes of the Trivandrum Block are seldom simply crystallised 'melts'. The leucogranites may vary in composition due to feldspar-controlled crystal fractionation and complementary crystal accumulation accompanied by drainage of fractionated melt, but more importantly they and the in-situ to near-situ leucosomes represent mixes of melt and minor to moderate proportions of a peritectic phase assemblage involving garnet, ilmenite and K-feldspar.

3. Cumulate leucogranites, accumulations of early-crystallised and/or peritectic feldspars and quartz, are characterised by highly positive Eu* at low total HREE, and low HFSE. They can be distinguished by their extremely low Zr that result in anomalous zirconium saturation temperatures.

4. Peritectic phase assemblage entrainment occurs quantitatively in the proportions in which the peritectic minerals a produced with melt, as predicted and modelled in recent studies (e.g. Taylor and Stevens, 2010). The proportions of peritectic garnet, K-feldspar and ilmenite

entrained in the Trivandrum Block example are in the approximate molar ratio 3.6:3:1, consistent with phase equilibrium of the migmatites at 860-900°C and 6-7 kbar.

5. The age-corrected (550 Ma) heat production of the crustal section now represented by the exposed Trivandrum Block, based on the weighted average of preserved migmatite, in-situ leucosomes and leucogranites of all types, was 1.7 ± 0.5 μWm^{-3}. Correction of the 550 Ma heat production to account for an estimated 30% of migration and loss of well-segregated leucogranites with higher heat productions (2.7±0.8 μWm^{-3}) from this middle crustal migmatite complex yields a syn-orogenic heat production of c. 2.0 ± 0.6 μWm^{-3}. Although elevated compared with model middle-crust, this heat production is unlikely to have been high enough to have facilitated the near-UHT to UHT metamorphism in the Trivandrum Block without the addition of heat external to the orogenic crust itself.

Acknowledgements

The study is a contribution to the PLAN 2020 project in the National Centre for Earth Science Studies, Thiruvananthapuram, Kerala, India. Work carried out by VN and SLH at the University of Edinburgh was supported by a grant from INSA (Indian National Science Academy) and a Royal Society of Edinburgh collaborative visiting fellowship. VN acknowledges the advice and support of Drs. M. Rajeevan and Shailesh Nayak, Ministry of Earth Sciences, Government of India; Drs.. M. Baba, N.P. Kurian and Virendra M. Tiwari, former directors of CESS / NCESS, Kerala; Prof. Somnath Das Gupta, Dr. B. K. Bansal, programme officer, MoES, and Prof. S.K. Tandon, (RAC, NCESS). VN is also indebted to Dr. N. Purnachandra Rao, Director, NCESS for his continuing support. The work benefitted from discussions with Drs. Sajeev Krishnan, Vinod Samuel, J.L. Jayanthi, J.K. Tomson, Nilanjana Sorcar. Kumar Batuk Joshi., Mrs. Sreejambika Sivaprasad and Mr. K. Eldhose. G. Stevens and an anonymous reviewer are thanked for their helpful and positive reviews.

Funding

INSA (Indian National Science Academy- Royal Society of Edinburgh) research grant to VN: 'Fluids, melts and chemical redistribution during high-grade metamorphism of the continental crust of southern India'

Declarations of Interest: None

References

Anders, E., Grevasse, N., 1989. Abundance of the elements: Meteoritic and Solar. Geochimica et Cosmochimica Acta 53, 197-214.

Bartlett, J.M., Dougherty-Page, J.S., Harris, N.B.W., Hawkesworth, C.J., Santosh, M., 1998. The application of single zircon evaporation and model Nd ages to the interpretation of polymetamorphic terrains: an example from the Proterozoic mobile belt of south India. Contributions to Mineralogy and Petrology 131, 181–195.

Beaumont, C., Ngugen, M.H., Jamieson, R.A., Ellis, S., 2006. Crustal flow modes in large hot orogens. In: Law, R.D., Searle, M.P. and Godin, L. (eds.) Channel Flow, Ductile Extrusion and Exhumation in Continental Collision Zones. Special Publication Geological Society of London 268, 91-145.

Blereau, E., Clark, C., Taylor, R.J.M, Johnson, T.E., Fitzsimons, I.C.W., Santosh, M., 2016. Constraints on the timing and conditions of high-grade metamorphism, charnockite formation and fluid-rock interaction in the Trivandrum Block, southern India. Journal of Metamorphic Geology 34, 527-549.

Braun, I., Bröcker, M., 2004. Geochronology of granitic gneisses and leucogranites from the Kerala Khondalite Belt, southern India: implications for late Proterozoic crustal evolution in east Gondwana. International Journal of Earth Sciences 93, 13–22.

Brown, M., 2004. The mechanism of melt extraction from lower continental crust of orogens. Transactions of the Royal Society of Edinburgh 95, 35-48.

Brown, M., 2013. Granite: from genesis to emplacement. Geological Society of America Bulletin doi:10.1130/B30877.1

Brown, M., Rushmer, T., 1997. The role of deformation in the movement of granite melt: views from the laboratory and the field. In: Holness M.B. (ed) Deformation-enhanced Fluid Transport in the Earth's Crust and Mantle (ed.). The Mineralogical Society Series 8 Chapman and Hall, London, pp. 111-144

Brown, M., Solar G.S., 1998, Granite ascent and emplacement during contractional deformation in convergent orogens; Journal of Structural Geology 20 1365-1393

Carvalho, B.B., Sawyer, E.W., Janasi, V.A., 2017. Enhancing maficity of granitic magma during anatexis: entrainment of infertile mafic lithologies. Journal of Petrology 58, 1333-1362.

Cenki, B., Braun, I., Bröcker, M., 2004. Evolution of the continental crust in the Pan-African mobile belt of southernmost India: evidence from Nd isotope mapping combined with U–Pb and Rb–Sr geochronology. Precambrian Research 134, 275–292.

Cenki, B., Kriegsman, L.M., Braun, I. 2002. Melt producing and melt consuming reactions in the Achankovil cordierite gneisses, southern India. Journal of Metamorphic Geology 20, 543-561.

Chacko, T., Ravindra Kumar, G.R., Newton R.C., 1987. Metamorphic P–T conditions of the Kerala (South India) Khondalite belt: a granulite-facies supracrustal terrain. Journal of Geology 96, 343–358.

Cesare, B., Ferrero, S., Salvioli-Mariani, E., Pedron, D., Cavallo, A., 2009. "Nanogranite" and glassy inclusions: the anatectic melt in migmatites and granulites. Geology 37, 627-630.

Clark, C., Fitzsimons, I.C.W., Healy, D., Harley, S.L., 2011. How does the continental crust get really hot? Elements 7, 235-240.

Clark, C., Healy, D., Johnson, T.E., Collins, A.S., Taylor, R.J.M., Santosh, M., 2015. Hot orogens and supercontinent amalgamation: a Gondwanan example using SHRIMP U–Pb

geochronology, REE geochemistry, phase equilibria and numerical modelling. Gondwana Research 28, 1310–1328.

Clauser. C., 2011. Radiogenic Heat Production of Rocks. Encyclopedia of Solid Earth Geophysics 2, 1-11.

Clemens, J.D., 2012. Granitic magmatism, from source to emplacement: a personal view. Applied Earth Science, Transactions Institute Mineralogy and Metallurgy B 121 (3), 107-136.

Clemens, J.D., Vielzeuf, D. 1987. Constraints on melting and magma production in the crust. Earth and Planetary Science Letters 86, 207-306.

Collins, A.S., Santosh, M., Braun, I., Clark, C., 2007. Age and sedimentary provenance of the Southern Granulites, South India: U-Th-Pb SHRIMP secondary ion mass spectrometry. Precambrian Research 155, 125-138.

Collins, A.S., Clark, C., Plavsa, D., 2014. Peninsula India in Gondwana: The tectonothermal evolution of the Southern Granulite Terrain and its Gondwanan counterparts. Gondwana Research 25, 190-203.

de Capitani, C., Petrakakis, K., 2010. The computation of equilibrium assemblage diagrams with Theriak/Domino software. American Mineralogist 95, 1006-1016.

Frost, B.R., Arculus, R.J., Barnes, C.G., Collins, W.J., Ellis, D.J., Frost, C.D., 2001. A geochemical classification of granitic rocks. Journal of Petrology 42, 2033-2048

Garcia-Arias, M., Stevens, G., 2017. Phase equilibrium modelling of granite magma petrogenesis: A. An evaluation of the magma compositions produced by crystal entrainment in the source. Lithos 277, 131-153.

Harley. S.L., 2016. A Matter of Time: The importance of the duration of UHT metamorphism. Journal of Mineralogical and Petrological Sciences 111, 50-72.

Harley, S.L., Nandakumar, V., 2014. Accessory mineral behaviour in granulite migmatites: A case study from the Kerala Khondalite Belt, India. Journal of Petrology 55, 1965-2002.

Harley, S.L., Nandakumar, V., 2016. New Evidence for Palaeoproterozoic high grade metamorphism in the Trivandrum Block, Southern India. Precambrian Research 280, 120-138

Harris, N.B.W., Santosh, M., Taylor, P.N., 1994. Crustal evolution in South India: constraints from Nd isotopes. Journal of Geology 102, 139-150.

James, R.S., Hamilton, D.L., 1969. Phase relationships in the system $NaAlSi_3O_8$-$KAlSi_3O_8$-$CaAl_2Si_2O_8$- SiO_2 at 1 kilobar water vapour pressure. Contributions to Mineralogy and Petrology 21, 111-141.

Jamieson, R.A., Beaumont, C., 2013. On the origin of orogens. Geological Society of America Bulletin 125, 1671-1702.

Johannes, W., Holtz, F., 1996. Petrogenesis and experimental petrology of granitic rocks. Berlin: Springer Verlag.

Johnson, T.E., White, R.W., Powell, R. 2008. Partial melting of metagreywacke: a calculated mineral equilibria study. Journal of Metamorphic Geology 26, 837-853.

Koester, E., Pawley, A.R., Fernandes, L.A., Porcher, C.C., Soliani, E., 2002. Experimental melting of cordierite gneiss and the petrogenesis of syntranscyrrent peraluminous granites in southern Brazil. Journal of Petrology 43, 1595-1616.

Kriegsman, L.M., 2001. Partial melting, partial melt extraction and partial back reaction in anatectic migmatites. Lithos 56, 75-96.

Kröner, A., Santosh, M., Wong, J., 2012. Zircon ages and Hf isotopic systematics reveal vestiges of Mesoproterozoic to Archaean crust within the late Neoproterozoic-Cambrian high-grade terrain of southernmost India. Gondwana Research 21, 876-886.

Kröner, A., Santosh, M., Hegner, E., Shaji, E., Geng, H., Wong, J., Xie, H., Wan, Y., Shang, C.K., Liu, D., Sun, M., Nandakumar, V., 2015. Palaeoproterozoic ancestry of Pan-African high-grade granitoids in southernmost India: Implications for Gondwana reconstructions. Gondwana Research 27, 1-37.

McLennan, S.M., 2001. Relationships between the trace element composition of sedimentary rocks and upper continental crust. Geochemistry Geophysics Geodynamics 2, paper 2000GC000109.

Melo, M.G., Stevens, G., Lana, C., Pedrosa-Soares, A.C., Frei, D., Alkmim, F.F., Alkmim, L.A., 2016. Repeated partial melting events in the Araçuaí orogeny southeastern Brazil): Evidence from the polymetamorphic Carlos Chagas Batholith. Lithos, 277, 51-71.

Morfin, S., Sawyer, E.W., Bandyayera, D., 2014. The geochemical signature of a felsic injection complex in the continental crust: Opinaca Subprovince, Quebec. Lithos 196–197, 339–355.

Morimoto, T., Santosh, M., Tsunogae, T., Yoshimura, Y., 2004. Spinel + quartz association from the Kerala Khondalites, southern India: evidence for ultrahigh-temperature metamorphism. Journal of Mineralogical and Petrological Sciences 99, 257-278.

Nandakumar, V., Harley, S.L., 2000. A reappraisal of the pressure-temperature path of granulites from the Kerala Khondalite Belt, southern India. Journal of Geology 108, 687-703.

Nicoli, G., Stevens, G., Moyen, J-F., Vezinet, A., Mayne, M., 2017. Insights into the complexity of crustal differentiation: K2O-poor leucosomes within metasedimentary migmatites from the

Southern Marginal Zone of the Limpopo Belt, South Africa. Journal of Metamorphic Geology 35, 999-1022.

Patiño-Douce, A.E. Harris, N.B.W., 1998. Experimental constraints on Himalayan anatexis. Journal of Petrology 39, 689-710.

Patiño-Douce, A.E., Johnston, A.D., 1991. Phase equilibria and melt productivity in the pelitic system: implications for the origin of peraluminous granitoids and aluminous granulites. Contributions to Mineralogy and Petrology 107, 202-218.

Pearce, J.A., Harris, N.B.W., Tindle, A.G., 1984. Trace element discrimination diagrams for the tectonic interpretation of granitic rocks. Journal of Petrology 25, 956-983.

Rudnick, R.L, Gao, S., 2003. In: Holland, H.D., Turekian, K.K. (eds.) Treatise of Geochemistry Volume 3: The Crust, Oxford UK Elsevier-Pergamon, pp 1-64.

Santosh, M., 1996. The Trivandrum and Nagercoil Granulite Blocks. Gondwana Research Group Memoir 3, 243-277.

Santosh, M., Collins, A.S., Morimoto, T., Yokoyama, K., 2005. Depositional constraints and age of metamorphism in southern India: U-Pb chemical (EPMA) and isotopic (SIMS) ages from the Trivandrum Block. Geological Magazine 142, 255-268.

Santosh, M., Maruyama, S., Sato, K., 2009. Anatomy of a Cambrian suture in Gondwana: implications for the timing of Gondwana assembly. Gondwana Research 16, 321-341.

Sawyer, E.W., 1994. Melt segregation in the continental crust. Geology 22, 1019-1022.

Sawyer, E.W., 1998. Formation and evolution of granitic magmas during crustal reworking: the significance of diatexites. Journal of Petrology 39 1147-1167.

Sawyer, E.W., 2001. Melt segregation in the continental crust: Distribution and movement of melt in anatectic rocks. Journal of Metamorphic Geology 18, 291-309

Shabeer, K.P., Satish-Kumar, M., Armstrong, R., Buick, I.S., 2005. Constraints on the timing of Pan-African granulite-facies metamorphism in the Kerala Khondalite Belt of Southern India: SHRIMP mineral ages and Nd isotope systematics. Journal of Geology 113, 95-106.

Skjerlie, K.P., Patiño-Douce, A.E., Johnston, A.D., 1993. Fluid-absent melting of a layered crustal protolith: implications for the generation of anatectic granites. Contributions to Mineralogy and Petrology 114, 365-378.

Solar, G.S., Brown, M., 2001. Petrogenesis of migmatites in Maine, USA: possible source of peraluminous leucogranite in plutons? Journal of Petrology 42, 789-823.

Stevens G., Villaros, A., Moyen, J-F., 2007. Selective peritectic garnet entrainment as the origin of geochemical diversity in S-type granites. Geology, 35: 9-12.

Tadokoro, H., Tsunogae, T., Santosh, M., 2008. Metamorphic P-T path of the eastern Trivandrum Granulite Block, southern India: implications for regional correlation of lower crustal fragments. Journal of Mineralogical and Petrological Sciences 103, 279-284.

Taylor. J., Stevens, G., 2010. Selective entrainment of peritectic garnet in S-type granitic magmas: evidence from Archaean mid-crustal anatectites. Lithos 120, 277-292.

Taylor, R.J.M., Clark, C, Fitzsimons, I.C.W., Santosh, M., Hand, M., Evans, N., McDonald, B., 2014. Post-peak, fluid-mediated modification of granulite facies zircon and monazite in the Trivandrum Block, southern India Contributions to Mineralogy and Petrology 168, 1-17.

Thompson, A.B., 1982. Dehydration melting of pelitic rocks and the generation of H2O-undersaturated granitic liquids. American Journal of Science 282, 1567-1595

Vanderhaeghe, O., 2009. Migmatites, granites and orogeny: Flow modes of partially-molten rocks and magmas associated with melt/solid segregation in orogenic belts. Tectonophysics 477, 119-134.

Vielzeuf, D., Clemens, J.D., Pin, C., Moinet, E., 1990. Granites, granulites and crustal differentiation. In Granulites and Crustal Evolution (ed. D. Vielzeuf and P. Vidal), pp. 59-85.

Vielzeuf, D., Holloway, J.R., 1988. Experimental determination of the fluid-absent melting relations in the pelitic system: consequences for crustal differentiation. Contributions to Mineralogy and Petrology 98, 257-276.

Villaros, A., Stevens, G., Moyen, J.-F., Buick, I., 2009. The trace element compositions of S-type granites: evidence for disequilibrium melting and accessory phase entrainment in the source. Contributions to Mineralogy and Petrology 158, 543–561.

Waters, D.J., 1988. Partial melting and the formation of granulite facies assemblages in Namaqualand, South Africa. Journal of Metamorphic Geology 6, 387-404.

Watson, E.B., Harrison, M., 1983. Zircon saturation revisited: temperature and composition effects in a variety of crustal magma types. Earth Planetary Science Letters 64: 295-304.

Weinberg, R.F., Searle, M.P., 1998. The Pangong injection complex, Indian Karakoram: A case of pervasive granite flow through hot viscous crust: Journal of the Geological Society of London 155, 883–891.

White, R.W., Powell, R., 2002. Melt loss and the preservation of granulite facies mineral assemblages. Journal of Metamorphic Geology, 20, 621-632.

Whitehouse, M.J., Ravindra-Kumar, G.R., Rimša, A., 2014. Behaviour of radiogenic Pb in zircon during ultrahigh-temperature metamorphism: an ion imaging and ion tomography case

study from the Kerala Khondalite Belt, southern India. Contributions to Mineralogy and Petrology 168, 1042-1059.

Yakymchuk, C., Brown, M. Ivanic, T., Korhonen, F.J., 2013. Leucosome distribution in migmatitic paragneiss and orthogneiss: a record of self-organised melt migration and entrapment in a heterogeneous partially-molten crust. Tectonophysics 603, 136-154.

Yakymchuk, C., Brown, M. Clark, C., Korhonen, F.J., Piccoli, C., Siddoway, C.S., Taylor, R.J., Vervoort, J.D., 2015. Decoding polyphase migmatites using geochronology and phase equilibria modelling. Journal of Metamorphic Geology 33, 203-230.

Yakymchuk, C., Clark, C., White, R.W., 2017. Phase relations, reactions sequences and petrochronology. Reviews in Mineralogy 83, 13-53.

Figure Captions

Figure 1: Geological map of the Kerala Khondalite Belt, southern India, including the Trivandrum Block (region dominated by the pink and grey colours) and Nagercoil Block (orange-coloured region at the southern tip of India). Locations of sample sites, with their three-letter abbreviated names, and main towns are shown for reference. Inset map shows the position of the KKB in southern India. Latitudes and longitudes of the sample sites are provided in Appendix A1.

Figure 2: Field photos from different sample locations.

(a) Typical quarry face showing intensely intercalated dark grey to blue-grey migmatitic pelitic and semi-pelitic gneisses with leucosomes that occur as pockets and patches and layer-parallel veins, and larger leucogranites that occur as sheets and partly transgressive veins that coalesce along their length.

(b) Patchy cordierite-rich leucosomes within migmatitic politic gneiss, Kairali quarry. Sampling sites for KAI-2 and KAI-3 are indicated. Pen is 15 cm long.

(c) Isolated, coarse garnet within a well-segregated leucosome, Kulappara quarry. The garnet, interpreted to be of peritectic origin, is partially rimmed by cordierite. This is interpreted to reflect reaction between garnet and melt during cooling with decompression. Site of sample KLP-2 indicated. Pen is 15 cm long.

(d) Garnet-bearing leucogranite sheet featuring a sharp contact with migmatitic pelitic gneiss, the sample site of KNJ-2, Kanjampara quarry. The leucogranitic sheet itself contains coarser peritectic and finer garnet in trails, and thin schlieren dominated by cordierite that has both replaced garnet and formed as separate grains. Pen is 15 cm long.

(e) Leucosome-rich migmatitic semipelitic gneiss cut by discordant 3-5 cm width leucogranite and aplitic sheets, Kannimala quarry. Site of sample KNN-2 indicated. Pen is 15 cm long.

(f) Migmatitic cordierite, orthopyroxene and spinel bearing granulite, Nellikala quarry. Leucosome occurs as an irregular patchwork and network. Site of sample NEL-1 indicated. Pen is 15 cm long.

(g) Migmatitic metapelite showing melt-rich domains (leucosomes) and restitic domains (rich in cordierite and sillimanite), Pallikal quarry. Porphyroblastic garnets within the leucosomes with several mineral inclusions attest to garnet growth associated with melting and melt migration. Note the intense high-grade strain, with the leucosome and restitic layers strung out to be parallel on the larger scale. Sample site for PLK-1 indicated. Pen is 15 cm long.

(h) Garnet-bearing leucogranite sheet within migmatitic gneiss, Pallikal quarry. Note the leucosome-hosted graphite flake on the left side. Note the foliae and schlieren of mafic material (Bt + Crd + Ilm) on the margins of the garnet-bearing leucosome. Sample site for PLK-3 indicated. Coin is 2 cm in diameter.

Figure 3: Harker-type oxide-SiO_2 diagrams illustrating the variations in the principal major element oxides for the four rock types distinguished in the text.

Figure 4: Normative and Component projections of major element compositions.

(a) Normative (wt%) quartz-albite-orthoclase (Qz-Ab-Or) diagram showing the compositions of all rock types in terms of their felsic components. Fields with increased densities of stipples express the frequency distribution of c. 1200 granitic rocks (Johannes and Holtz, 1996). The star symbol represents the experimental minimum melt piercing point in the system Ab-Or-Q-H_2O at 1 kbar water pressure and 5 wt% An in the system (James & Hamilton, 1969).

(b) Normative (wt%) quartz-plagioclase-orthoclase Qz-Plag-Or diagram showing the compositions of all rock types in terms of their felsic components. Fields with increased densities of stipples express the frequency distribution of c. 1200 granitic rocks (Johannes and Holtz, 1996). Note the offset of the migmatites and restitic gneisses towards the Plag apex, removing them from the highest density field of granite compositions compared with figure 4(a). The star symbol represents the experimental minimum melt piercing point in the system Ab-Or-Q-H_2O at 1 kbar water pressure and 5 wt% An in the system (James & Hamilton, 1969).

(c) AFM diagram projected from Qz and Kfs (K-feldspar) as well as Ab and An normative components, showing the position of the projected bulk rock compositions of all rock types in terms of potential constituent AFM minerals (Sil, Grt, Crd, Bt/Opx), uncorrected for Ti that may be present in Ilmenite. Compositional fields for Grt, Bt and Crd are based on the mineral compositions reported in previous studies (Nandakumar & Harley, 2000; Braun & Bröcker, 2004). Compositional fields for peraluminous experimental melts produced by Skjerlie et al. (1993) and Koester et al. (2002) are shown by the shaded elliptical fields. Most leucogranites lie on or near a control line between sillimanite or experimental melt compositions and garnet (garnet control). Projected leucosome compositions lie near garnet. Most migmatites and restites are more magnesian and hence plot in or near the three-phase triangle Grt+Crd+Bt (or Opx).

Figure 5: Classification of leucogranites and leucosomes based on major element parameters, based on the discrimination criteria of Frost et al. (2001).

(a) A/NK versus ASI (alumina saturation index) of leucogranites and leucosomes (see Table 1 for data). Both rock types plot within the field of peraluminous granitoids.

(b) FeO(total)/[FeO(total)+MgO] versus SiO_2 of leucogranites and leucosomes (see Table 1 for data). Most samples are ferroan or straddle the ferroan-magnesian boundary.

Figure 6: Fe_2O_3 and selected transition metals (V, Cr, Co, Ni, Zn) and HFSE (Nb, Zr) plotted against TiO_2 for all rock types. Note the strong correlations of Fe_2O_3, V, Co and Nb with TiO_2 for the leucogranites and leucosomes compared with the scatter recorded from migmatites and restites. Cr is similar for all rock types. Control lines for ilmenite (Ilm), garnet (Grt) and, in the case of Fe_2O_3, biotite (Bt) are shown. See text for discussion.

Figure 7: Ni (a) and Zn (b) plotted against Fe_2O_3 for all rock types. Note the strong correlation of Ni and, to a lesser extent, Zn with Fe_2O_3 for the migmatites and restites. This is interpreted to reflect the role of sulphide and magnetite in these rocks. See text for discussion.

Figure 8: Rb (a, b) and Sr (c, d) variations between rock types plotted against SiO_2 (a, c) and K_2O (b) or CaO (d). Rb, higher in the leucogranites and leucosomes, correlated strongly with K_2O, whereas Sr, which is scattered but overall lower in the leucogranites and leucosomes correlated broadly with CaO. See text for discussion.

Figure 9: Spider diagrams for leucogranites (a), leucosomes (b), migmatites (c) and restites (d) showing trace element variations normalized against the average model middle crust of Rudnick and Gao (2003). The normalised trace element pattern for the post-Archaean average Australian shale composite (PAAS), average greywackes and average arenites from McLennan (2001) are shown for comparison. Note the extreme relative depletions in Cs and Cu in all rock types, and overall relative depletions in the transition metals and Zr in most rocks relative to middle crust and PAAS. Leucogranites (a) are divided into two groups: those with positive Eu anomalies are denoted by the black lines, and those that feature negative Eu anomalies by the grey lines. Low-Nb samples KNJ3 and KLP1 are discussed in the text.

Figure 10: Chondrite-normalised REE patterns for leucogranites (a), leucosomes (b) and migmatites and restites (c). Chondrite values are from Anders and Grevasse (1989). Leucogranites (a) are divided into two groups: those with positive Eu anomalies are denoted by the black lines, and those that feature negative Eu anomalies by the grey lines. The field of the latter sub-group is shaded pale grey, and this field is shown on the leucosome diagram (b). The average REE pattern for the post-Archaean average Australian shale composite (PAAS: McLennan, 2001) is shown as the red line in (c). Leucogranite KNJ3 is discussed in the text.

Figure 11: Y (a) and Dy (b) plotted against Fe_2O_3 for all rock types. Note the strong correlation of Y and Dy with Fe_2O_3 for the leucosomes and many of the leucogranites, in contrast to the scatter exhibited by the migmatites and restites. The pale pink field in each diagram is the garnet control line, with garnet Y and Yb contents constrained at high Fe_2O_3 by the SIMS garnet analyses of Harley and Nandakumar (2014, 2016). Leucogranite PLK2, discussed later in the text, is distinguished by its low Dy and Y at moderate Fe_2O_3.

Figure 12: Zr contents in all rock types plotted against SiO2 (a), and Zr contents plotted against Nb+Y (b) and the Eu anomaly, Eu*, for leucosomes and leucogranites. Three digit figures in (b) and (c) are zirconium saturation temperatures for each rock, calculated from the calibration of Watson and Harrison (1983) and listed in Table 4. The grey shaded field in (b) shows the Zr vs Nb+Y field defined by the leucogranites with positive Eu*. The vector on this diagram shows the effect of increasing garnet + ilmenite. Leucogranite KNJ3, which has very low Nb+Y and Zr, and a strongly positive Eu*, is highlighted in (c).

Figure 13: Heat productions, at 550 Ma, of Trivandrum Block samples, calculated from measured Th, U and K_2O contents corrected for bulk densities determined from normative mineralogy (Table 5).

(a) Heat productions at 550 Ma, in μWm^{-3}, plotted against combined Th+U. Leucogranites spread from low Th+U similar to migmatites, up to higher Th+U overlapping with leucosomes.

(b) Heat productions for leucogranites and leucosomes at 550 Ma, in μWm^{-3}, plotted against combined Nb+Y, interpreted as a measure of entrained or incorporated ilmenite and garnet. There is a broad overall correlation between the two.

Figure 14: Molar Fe+Mg+Ti – Na+Ca – K diagram after Solar and Brown (2001), depicting the molar proportions of felsic (Na+Ca, K) components versus amfic (Fe+Mg+Ti) components in all rock samples from the Trivandrum Block. The positions of key minerals – garnet (Grt), cordierite (Crd), ilmentite (Ilm), biotite (Bt), K-feldspar (Kfs) and plagioclase (Plag) – are show along with a biotite-plagioclase reference tie line. Compositions of experimental melts produced from pelites (Patino Douce and Harris, 1998; Koester et al., 2002) and a layered greywacke (Skerjlie et al, 1993) are shown as coloured elliptical fields, along with the compositions of the starting materials as coloured star symbols. Leuocgranites plot in or around the experiemental fields, with four plotting to lower Fe+Mg+Ti. Leucosomes lie one or to the plagioclase side of a control line between the extreme leucogranite compositions and garnet. See text for further discussion.

Figure 15: Log-log Trace element discrimination diagrams (TEDDs; Pearce et al. 1984) illustrating key trace element variations in Trivandrum Block leucogranites and leucosomes. The grey shaded field in all diagrams is that corresponding to migmatites and restites. VAG is ‘volcanic arc granite’; COLG is ‘collisional granite’; WPG is ‘within plate granite; and ORG is ‘ocean ridge granite’. See discussion in the text for the relevance of these tectonic setting inferences.

(a) And (b) Rb plotted against Y+Nb and Ta+Yb respectively. Rb is similar in all samples. The effect of garnet + ilmenite addition is shown by the Grt + Ilm vectors. Samples KNJ3 and KLP1, discussed in the text, are highlighted.

(c) Ta versus Yb. Ta-Yb compositions of ilmenite (blue square) and garnet (pink square) are from Harley and Nandakumar (2014) or extrapolated from Ta versus TiO_2 correlations. These produce the garnet:ilmenite mixing curve shown contoured for wt% ilmenite (20, 15, 10, 5 wt%).Most leucogranites and leucosomes form a linear array that corresponds to the addition of garnet and ilmenite in the proportions 7-8 wt% ilmenite:92-93 wt% garnet (dashed line). Samples KNJ3 and KLP1, discussed in the text, are highlighted.

(d) Nb versus Y. Nb-Y compositions of ilmenite (blue square) and garnet (pink square) are from Harley and Nandakumar (2014) or extrapolated from Nb versus TiO_2 correlations. These produce the garnet:ilmenite mixing curve shown contoured for wt% ilmenite (20, 15, 10, 5 wt%). Most leucogranites and leucosomes form a linear array that corresponds to the addition of garnet and ilmenite in the proportions 6-7 wt% ilmenite:93-94 wt% garnet (dashed line). Samples KNJ3 and KLP1, discussed in the text, are highlighted.

Figure 16: Log-log Trace element diagrams depicting the variations between Sr and Ba (a) and Ba versus Nb+Y (b) in Trivandrum Block leucogranites and leucosomes.

(a) Sr-Ba plot. Data for leucogranites from the Opinaca migmatite / injection complex (Morfin et al., 2014) are shown by the shaded field. Crystal fractionation control on Opinaca leucogranite Sr-Ba chemistry as modelled by Morfin et al. (2014) is shown by the 'Opinaca trend' (dashed line with 10% contours), with a starting liquid at the pale grey shaded square. Leucogranites and leucosomes from the Trivandrum lie of steeper trends, with two trends evident: one at lower-Ba (4 samples), and the other at higher-Ba

for a given Sr. Three model melt fractionation trends for Trivandrum Block leucogranites are contoured for up to 30% fractionated feldspars, for either 100% Kfeldspar (black-filled diamond symbols), 50:50 wt% Kfeldspar and plagioclase (blue-filled diamond symbols), or 30 wt% Kfeldspar : 70 wt% Plagioclase (purple-filled diamond symbols), from an assumed model starting melt at the grey diamond (solid curves to low Sr-Ba). The lower Sr-Ba subgroup of leucogranites lie on a trend (fine dashed line) parallel to the 50:50 wt% Kfeldspar and plagioclase fractionation model. Leucogranite PLK2 lies at the most fractionated end of this trend. Feldspar accumulation and/or incorporation mixing lines are shown from the same starting composition up to 15wt% Kfeldspar alone (black-filled circle symbols), and 20 wt% total of 50:50 Kfeldspar and plagioclase (blue-filled circle symbols). Leucogranites KNJ3 and KNJ1, discussed in the text, lie at the upper end of these mixing lines.

(b) Ba plotted against Nb+Y for leucogranites and leucosomes. The low Sr-Ba subgroup of leucogranites identified in (a) and trending down to sample PLK2, lie at moderate Nb+Y, whereas leucogranites with higher Ba range in Nb+Y from those with higher Nb+Y similar to leucosomes (red diamonds) to three with low to very low Nb+Y. The latter group includes leucogranites KNJ3, KLP1 and KNJ1, all of which have strong positive Eu* anomalies.

Table A1: Sample location and rock types (excel file)

Table A2: Summary of all Chemical Data (excel file)

Table 1: Major element compositions of Trivandrum Block Samples (a) leucogranites and leucosomes

Sample	KLP-1	KAl-3	KNJ-1	PLK-3	PLK-1	KBL-1	KLP-3	PLK-2	KNJ-3	MLK-3	KBL-3	KNN-2	KTP-2	MLK-1	MLK-2	KNN-1A	KNN-3
Rock type	LG	LG	LG	LG	LG	LG	LG	LG	LG	LG	LG	LG	LG	LS	LS	LS	LS
SiO_2	74.93	74.49	74.45	74.28	73.85	73.47	73.30	73.27	72.73	72.15	71.32	71.08	70.28	68.99	68.84	68.97	68.88
TiO_2	0.03	0.11	0.02	0.22	0.11	0.17	0.37	0.18	0.02	0.22	0.36	0.30	0.33	0.82	0.96	0.50	0.62
Al_2O_3	14.73	14.51	14.80	14.42	14.33	15.07	14.01	15.18	16.22	14.14	15.45	15.14	15.70	14.62	14.41	15.33	15.25
Fe_2O_3	1.19	1.50	0.59	1.02	1.51	1.75	2.29	2.67	0.50	2.13	3.01	2.51	2.22	4.90	5.52	3.35	4.65
MnO	0.02	0.01	0.01	0.01	0.01	0.02	0.03	0.01	0.00	0.03	0.04	0.03	0.04	0.06	0.08	0.03	0.06
MgO	0.17	0.25	0.14	0.12	0.23	0.38	0.48	0.38	0.06	0.18	0.82	0.44	0.74	0.61	0.71	0.81	0.90
CaO	0.67	1.18	0.79	0.76	1.16	0.68	1.21	0.79	1.07	1.35	0.54	1.38	1.65	2.04	2.07	1.85	2.05
Na_2O	2.67	3.15	2.84	3.00	3.10	3.08	2.73	2.61	3.32	2.20	2.53	1.86	3.43	2.75	2.77	2.75	2.08
K_2O	5.53	4.70	5.76	5.73	4.70	5.13	4.72	4.38	5.85	6.58	5.36	6.54	5.11	4.67	4.05	5.60	4.71
P_2O_5	0.14	0.14	0.10	0.09	0.13	0.13	0.10	0.13	0.16	0.82	0.12	0.22	0.10	0.27	0.25	0.18	0.23
Total	100.05	100.04	99.50	99.64	99.12	99.88	99.22	99.59	99.94	99.80	99.55	99.50	99.60	99.73	99.66	99.37	99.43
ASI	1.28	1.18	1.21	1.16	1.18	1.28	1.20	1.46	1.19	1.08	1.43	1.21	1.12	1.11	1.14	1.11	1.25
A/	1.43	1.	1.	1.31	1.42	1.	1.4	1.	1.39	1.3	1.57	1.	1.42	1.54	1.	1.46	1

NK		43	37			43	8	70		3		51			63		.81
F/F+M	0.86	0.85	0.79	0.88	0.86	0.81	0.81	0.86	0.88	0.91	0.77	0.84	0.73	0.88	0.87	0.79	0.82
***X_{Mg}**	22.6	26.1	32.8	22.9	24.3	32.4	33.4	23.2	20.9	15.8	38.2	28.6	43.9	23.0	23.7	36.2	30.8
****A/AFM**	62.7	47.9	70.3	59.7	47.7	52.6	38.5	53.7	76.9	33.6	45.6	40.4	27.4	18.5	19.9	21.1	30.0
Normative Components																	
Apat	0.07	0.08	0.06	0.05	0.07	0.07	0.05	0.07	0.10	0.47	0.07	0.13	0.06	0.16	0.15	0.11	0.13
Ilm	0.04	0.17	0.03	0.33	0.16	0.25	0.54	0.24	0.03	0.34	0.53	0.47	0.56	1.32	1.49	0.85	0.93
Opx	2.2	2.8	1.3	1.6	2.8	3.5	4.2	4.5	1.0	3.5	6.4	4.8	5.8	8.6	9.4	7.7	8.9
An	1.0	2.1	1.4	1.4	2.1	1.1	2.2	1.2	2.0	0.6	0.8	2.4	3.7	3.9	3.9	3.9	3.8
Ab	9.9	12.0	11.0	11.8	11.9	11.8	10.3	9.3	14.0	8.9	9.6	7.4	15.1	11.4	11.1	12.1	8.1
Or	13.2	11.5	14.4	14.6	11.6	12.7	11.5	10.0	15.9	16.8	13.2	16.9	14.5	12.5	10.5	15.9	11.8
Qz	69.6	68.5	68.5	67.5	68.6	66.3	68.3	69.2	63.2	66.0	63.7	64.1	57.7	59.6	60.6	56.9	62.1
Crn	4.0	2.9	3.3	2.7	2.9	4.2	2.9	5.5	3.8	3.6	5.7	3.8	2.5	2.6	2.9	2.6	4.3
sum	100	100	100	100	100	100	100	100	100	100	100	100	100	100	100	100	100

* LG: leucogranite; LS: leucosome

*** X_{Mg}**: molar ratio, corrected for ilmenite; = 100*[(Fe-Ti)/(Fe-Ti+Mg)]

**** A/AFM**: molar ratio, A corrected for K, Na and Ca; Ca corrected for P; Fe corrected for ilmenite; $A = Al_2O_3-K_2O-Na_2O-CaO+(1.666*P_2O_5)$

Table 1: Major element compositions of Trivandrum Block Samples (b) migmatites and restites

Sample	KLP-2	CKL-3	KAI-5	ASM-2	CKL-1	NEL-1	NEL-2	KAI-2	KAI-4	KNJ-2	KBL-2	NEL-4	ASM-1	CKL-2	KTP-1
Rock type	Mig	Mig	Mig	Mig	Mig	Mig	Mig	Mig	Mig	Mig	Mig	Rest	Rest	Rest	Rest
SiO_2	66.20	65.69	65.55	65.45	63.88	63.39	62.56	62.51	62.31	61.94	61.83	59.66	59.27	58.18	57.65
TiO_2	0.67	0.61	0.74	0.75	0.91	0.92	1.27	1.10	0.96	0.73	0.70	1.16	1.03	0.58	1.13
Al_2O_3	16.03	17.52	15.42	16.37	17.92	16.81	14.43	18.01	15.82	18.67	19.83	17.11	19.59	20.83	18.15
Fe_2O_3	6.58	4.59	5.66	5.49	6.21	6.40	8.23	7.87	7.21	7.43	9.55	7.37	6.57	7.05	5.39
MnO	0.09	0.06	0.05	0.06	0.10	0.14	0.07	0.14	0.07	0.08	0.16	0.11	0.06	0.07	0.20
MgO	1.69	1.72	1.80	1.85	2.48	2.39	2.95	2.88	2.28	2.12	1.30	2.04	1.81	2.56	2.42
CaO	1.16	2.68	2.64	2.65	2.72	2.57	2.99	3.33	3.72	1.14	1.07	2.72	4.59	3.32	4.25
Na_2O	2.33	3.24	3.27	3.62	3.16	3.10	3.30	4.27	3.41	2.39	2.21	3.50	5.26	3.88	3.98
K_2O	3.25	3.26	2.66	3.30	2.27	3.29	1.64	2.90	1.93	3.53	2.19	4.37	1.51	3.07	4.66
P_2O_5	0.07	0.00	0.05	0.10	0.00	0.06	0.05	0.05	0.03	0.07	0.00	0.07	0.09	0.00	1.75
Total	98.07	99.37	97.84	99.64	99.65	99.08	97.49	103.07	97.75	98.11	98.84	98.11	99.78	99.54	99.58
ASI	1.71	1.28	1.19	1.15	1.43	1.27	1.14	1.11	1.10	1.92	2.51	1.12	1.05	1.33	0.94
A/NK	2.20	1.99	1.88	1.73	2.36	1.95	2.01	1.78	2.06	2.43	3.33	1.65	1.91	2.16	1.58
F/F+M	0.78	0.71	0.74	0.73	0.69	0.71	0.72	0.71	0.74	0.76	0.87	0.76	0.77	0.71	0.67
*X_{Mg}	36.4	46.3	42.3	43.8	48.3	46.6	45.8	45.9	42.2	38.7	22.7	39.6	39.5	44.1	53.2
**A/AFM	36.0	28.9	18.4	16.6	29.1	21.4	10.3	10.6	9.5	39.0	44.9	12.0	8.6	25.9	-0.3
Normative Components															
Apat	0.04	0.00	0.03	0.07	0.00	0.04	0.03	0.04	0.02	0.04	0.00	0.06	0.08	0.00	1.56
Ilm	1.0	1.0	1.2	1.3	1.5	1.6	2.1	2.2	1.7	1.1	1.0	2.5	2.4	1.2	2.7
Opx	13.4	12.5	14.1	15.0	16.5	18.0	21.7	25.5	19.4	17.0	16.1	22.7	21.7	24.7	22.0
An	2.2	6.4	6.1	6.4	6.2	6.2	7.0	9.4	9.4	2.3	2.1	8.2	15.1	10.1	6.6
Ab	8.6	14.0	13.9	16.5	13.1	13.9	14.3	22.2	15.8	9.5	7.9	19.7	32.0	21.3	24.4
Or	7.8	9.1	7.3	9.7	6.1	9.5	4.6	9.8	5.8	9.1	5.1	15.9	5.9	10.9	18.4
Qz	59.4	51.9	54.1	47.8	49.9	45.8	47.7	27.8	45.8	50.0	54.9	27.6	20.5	23.4	18.6
Crn	7.7	5.1	3.3	3.2	6.7	5.0	2.6	3.1	2.1	11.0	13.0	3.3	2.2	8.6	5.8
sum	100	100	100	100	100	100	100	100	100	100	100	100	100	100	100

* Mig: migmatitic gneiss; Rest: restitic gneiss

*** X_{Mg}**: molar ratio, corrected for ilmenite; = 100*[(Fe-Ti)/(Fe-Ti+Mg)]

**** A/AFM**: molar ratio, A corrected for K, Na and Ca; Ca corrected for P; Fe corrected for ilmenite; A = Al_2O_3-K_2O-Na_2O-CaO+(1.666*P_2O_5)

Table 2: Trace element compositions of Trivandrum Block Samples (a) leucogranites and leucosomes

Sample	KLP-1	KAI-3	KNJ-1	PLK-3	PLK-1	KBL-1	KLP-3	PLK-2	KNJ-3	MLK-3	KBL-3	KNN-2	KTP-2	MLK-1	MLK-2	KNN-1A	KNN-3
Rock type	LG*	LG	LG	LG	LG	LG	LG	LG	LG	LG	LG	LG	LG	LS*	LS	LS	LS
Sc	3.1	2.6	2.3	3.0	3.0	12.8	3.3	2.8	2.1	3.4	3.5	3.2	3.4	4.5	4.5	3.1	3.9
V	3.8	3.2	2.3	3.7	4.3	3.7	5.8	3.4	2.5	4.1	5.6	5.3	6.8	5.3	5.4	5.2	7.2
Cr	12.8	11.7	10.0	11.7	13.4	12.6	13.0	10.4	12.4	15.2	10.5	9.6	13.7	11.0	12.9	11.0	12.9
Co	1.6	2.1	0.6	1.8	2.0	3.0	4.0	1.2	0.5	3.2	7.9	4.2	4.1	8.0	8.2	6.4	7.8
Ni	0.9	1.2	0.8	1.6	1.3	1.4	1.4	0.7	0.7	1.1	3.0	1.2	1.4	1.5	1.3	1.8	1.8
Cu	0.4	0.6	0.3	0.7	0.6	1.7	0.5	0.2	0.3	0.5	1.0	0.6	0.8	0.6	0.6	1.0	0.9
Zn	12.2	12.2	16.0	12.0	29.2	23.6	12.6	17.3	15.5	16.1	16.9	15.8	12.1	29.1	25.2	26.7	25.9
Ga	14.4	16.9	14.0	17.6	16.3	15.0	18.0	10.5	12.7	18.1	15.2	15.8	15.7	19.5	17.5	19.3	18.1
Rb	216	201	172	237	187	171	196	111	206	395	212	268	120	181	145	243	188
Sr	156	85	207	80	58	158	205	21	187	104	87	106	214	108	100	149	122
Y	5.6	11.1	6.5	6.0	9.8	10.2	13.4	6.6	1.2	27.8	32.9	19.1	13.8	40.4	39.2	29.2	33.8
Zr	62	9	21	47	8	86	44	85	4	67	197	31	71	181	157	67	62
Nb	0.4	4.2	1.2	6.0	4.0	4.0	7.7	8.3	0.6	6.7	10.2	8.2	6.2	17.9	17.9	13.6	13.3
Ta	0.0	0.2	0.2	0.3	0.3	0.1	0.4	0.5	0.0	0.5	0.5	0.4	0.2	1.0	1.1	0.6	0.7
Cs	0.7	0.7	0.9	0.3	0.7	0.1	0.3	0.2	0.7	0.7	0.2	0.6	0.2	0.2	0.2	0.9	0.6
Ba	807	194	1112	659	149	309	1085	70	614	684	619	962	1150	656	559	1031	824
U	1.1	0.5	0.7	2.1	0.3	2.9	1.6	4.4	1.1	7.8	4.5	2.3	1.0	3.9	2.0	2.7	2.9
Th	5.4	0.3	0.4	21.9	0.4	7.8	31.7	8.1	2.5	2.4	15.3	7.1	36.2	28.0	18.7	47.0	35.4
Rb/Cs	316	289	190	775	273	1185	620	510	294	535	1175	414	797	861	819	257	309
Ba/Sr	5.2	2.3	5.4	8.2	2.6	2.0	5.3	3.4	3.3	6.6	7.1	9.0	5.4	6.1	5.6	6.9	6.7
Sr/Y	27.8	7.7	31.8	13.4	5.9	15.4	15.3	3.2	157.3	3.7	2.6	5.6	15.5	2.7	2.5	5.1	3.6
Zr/Y	168.4	2.1	18.5	7.8	2.0	21.5	5.8	10.2	6.2	10.0	19.2	3.8	11.5	10.1	8.8	4.9	4.7
Th/U	4.9	0.7	0.6	10.5	1.4	2.6	19.7	1.8	2.4	0.3	3.4	3.1	37.3	7.2	9.5	17.2	12.2
Nb/Ta	7.6	17.2	7.1	19.9	16.0	34.5	17.5	15.9	13.5	13.4	20.8	19.0	29.6	17.3	15.9	21.0	19.4
Y+Nb	6.0	15.3	7.7	12.0	13.9	14.2	21.1	14.9	1.8	34.5	43.1	27.2	20.0	58.2	57.0	42.8	47.1

* LG: leucogranite; LS: leucosome

Table 2: Trace element compositions of Trivandrum Block Samples (b) migmatites and restites

Sample	KLP-2	CKL-3	KAI-5	ASM-2	CKL-1	NEL-1	NEL-2	KAI-2	KAI-4	KNJ-2	KBL-2	NEL-4	ASM-1	CKL-2	KTP-1
Rock type	Mig*	Mig	Mig	Mig	Mig	Mig	Mig	Mig	Mig	Mig	Mig	Rest*	Rest	Rest	Rest
Sc	5.5	4.4	4.5	3.5	6.3	6.4	5.0	6.8	4.4	5.1	7.1	5.8	4.4	4.2	7.1
V	12.8	10.4	10.8	7.2	18.2	17.9	26.6	16.9	13.4	8.9	8.9	25.1	12.3	16.8	10.4
Cr	13.2	11.3	11.8	9.8	12.4	12.6	13.5	10.8	11.2	11.4	12.0	11.9	12.5	11.7	11.9
Co	16.5	11.2	11.5	5.7	17.2	15.6	17.6	19.5	16.3	19.6	21.6	17.5	13.0	15.7	12.3
Ni	6.6	2.7	3.2	1.3	4.4	3.8	6.3	4.0	4.3	6.7	11.1	4.7	3.2	4.2	2.9
Cu	1.3	1.6	0.8	0.5	0.8	0.5	1.3	0.5	3.4	1.9	3.0	1.4	1.3	0.7	1.3
Zn	32.0	40.4	21.3	14.9	46.6	21.3	115.7	28.3	26.1	31.8	30.0	52.4	34.5	41.5	23.0
Ga	18.1	18.8	20.6	8.0	18.9	20.4	25.1	26.2	24.4	19.0	21.5	26.2	17.7	27.2	17.2
Rb	158	78	65	9	57	116	30	57	53	143	64	202	96	65	107
Sr	130	295	195	105	245	218	208	256	318	178	74	238	264	345	253
Y	41	36	16	11	28	44	7	46	5	40	73	18	28	22	97
Zr	120	40	98	21	43	34	19	69	55	105	122	35	64	28	52
Nb	15.7	6.7	11.1	6.6	9.0	14.1	15.8	20.0	9.7	9.7	22.5	23.6	11.8	6.0	18.8
Ta	0.8	0.3	0.4	0.3	0.3	0.9	0.7	0.7	0.3	0.6	1.2	0.8	0.5	0.2	0.7
Cs	0.3	0.1	0.1	0.0	0.2	0.3	0.1	0.1	0.1	0.6	0.1	1.6	0.1	0.2	0.2
Ba	588	1272	555	127	640	836	402	516	1045	779	177	1043	769	1051	783
U	2.7	0.6	0.8	0.3	0.4	0.9	0.5	0.5	0.3	1.6	2.5	1.0	1.2	1.0	1.4
Th	10.0	8.0	16.8	3.9	2.9	6.6	1.0	2.7	9.4	9.3	15.7	4.8	8.9	7.0	4.2
Rb/Cs	462	764	843	248	267	439	490	893	472	252	532	122	664	391	481
Ba/Sr	4.5	4.3	2.8	1.2	2.6	3.8	1.9	2.0	3.3	4.4	2.4	4.4	2.9	3.0	3.1
Sr/Y	3.2	8.1	12.2	9.7	8.7	4.9	30.3	5.5	63.4	4.4	1.0	12.9	9.3	15.9	2.6
Zr/Y	7.6	6.0	8.9	3.2	4.8	2.4	1.2	3.4	5.7	10.8	5.4	1.5	5.4	4.7	2.8
Th/U	3.7	13.3	21.3	12.6	7.9	7.6	2.2	6.0	34.3	5.8	6.2	4.8	7.6	6.7	3.0
Nb/Ta	18.9	25.1	30.2	24.7	26.6	15.8	24.2	30.4	29.3	17.1	19.3	27.9	24.3	27.7	25.8
Y+Nb	56.9	43.1	27.1	17.3	37.3	58.4	22.7	66.5	14.7	49.8	95.8	42.0	40.1	27.8	115.5

* Mig: migmatitic gneiss; Rest: restitic gneiss

Table 3: Rare Earth Element compositions of Trivandrum Block Samples. (a) leucogranites and leucosomes

Sample	KLP-1	KAI-3	KNJ-1	PLK-3	PLK-1	KBL-1	KLP-3	PLK-2	KNJ-3	MLK-3	KBL-3	KNN-2	KTP-2	MLK-1	MLK-2	KNN-1A	KNN-3
Rock type	*LG	LG	LG	LG	LG	LG	LG	LG	LG	LG	LG	LG	LG	LS*	LS	LS	LS
La	11	9	6	79	8	27	92	20	10	63	47	38	126	93	71	116	98
Ce	21	16	10	136	15	58	177	43	19	152	101	74	241	194	146	250	208
Pr	2.0	1.5	1.0	13.1	1.4	6.2	18.0	4.6	2.0	18.1	11.0	7.8	23.8	20.5	16.0	27.8	23.3
Nd	7.2	5.1	3.4	45.4	5.1	23.4	63.5	17.2	7.4	74.1	42.5	30.1	83.2	77.5	60.5	105.7	88.3
Sm	1.2	0.9	0.7	6.5	0.9	4.8	8.8	3.9	1.3	14.6	8.9	6.2	11.6	12.7	10.4	17.9	15.0
Eu	1.03	0.43	0.73	0.84	0.44	0.58	1.48	0.18	0.85	1.30	0.89	1.37	1.43	1.13	0.95	1.55	1.40
Gd	0.77	0.89	0.63	3.91	0.85	3.31	5.41	2.81	0.79	9.56	6.82	4.49	8.36	9.24	8.14	11.86	9.96
Tb	0.11	0.19	0.12	0.34	0.18	0.44	0.55	0.39	0.08	1.15	0.99	0.64	0.87	1.25	1.14	1.35	1.24
Dy	0.81	1.52	0.94	1.22	1.44	2.19	2.48	1.70	0.29	5.41	5.79	3.58	3.57	7.11	6.98	6.11	6.52
Ho	0.09	0.20	0.12	0.11	0.18	0.19	0.26	0.12	0.02	0.53	0.61	0.37	0.29	0.76	0.76	0.59	0.65
Er	0.36	0.70	0.39	0.44	0.58	0.51	0.90	0.31	0.08	1.80	1.97	1.23	0.87	2.64	2.46	1.87	2.14
Tm	0.06	0.09	0.06	0.04	0.08	0.05	0.09	0.03	0.01	0.23	0.24	0.16	0.07	0.32	0.32	0.20	0.25
Yb	0.64	0.90	0.59	0.40	0.76	0.48	0.99	0.26	0.11	2.21	2.27	1.56	0.67	3.23	3.18	1.88	2.36
Lu	0.11	0.15	0.10	0.05	0.12	0.07	0.15	0.04	0.02	0.36	0.34	0.25	0.10	0.52	0.54	0.29	0.37
chondrite normalised REE																	
La	46.3	36.7	23.7	335.9	35.2	113.8	391.4	87.1	40.5	270.4	201.7	163.2	537.1	396.8	301.6	495.8	416.5
Ce	34.1	25.8	17.0	226.1	24.7	96.7	292.8	70.9	31.5	251.8	167.8	123.0	398.8	321.2	241.9	413.9	345.1
Pr	23.0	16.4	10.9	147.1	16.2	69.7	201.8	51.5	22.2	203.4	123.4	88.0	266.9	229.9	179.1	312.1	261.5
Nd	15.8	11.3	7.4	100.3	11.2	51.8	140.3	37.9	16.3	163.8	93.9	66.6	184.0	171.2	133.6	233.6	195.1
Sm	8.1	6.4	4.5	44.1	6.1	32.6	59.9	26.2	9.1	99.4	60.7	42.2	78.7	86.2	70.8	121.6	101.8
Eu	18.5	7.7	13.0	15.1	7.9	10.3	26.3	3.3	15.2	23.1	15.8	24.4	25.5	20.2	17.0	27.7	24.9
Gd	3.9	4.5	3.2	19.9	4.3	16.8	27.5	14.3	4.0	48.6	34.7	22.8	42.5	47.0	41.4	60.3	50.6
Tb	3.0	5.3	3.2	9.4	4.8	12.0	15.3	10.7	2.1	31.8	27.2	17.7	23.8	34.5	31.5	37.1	34.2
Dy	3.3	6.3	3.9	5.0	5.9	9.0	10.2	7.0	1.2	22.3	23.9	14.7	14.7	29.3	28.7	25.2	26.9
Ho	1.7	3.6	2.1	2.0	3.2	3.5	4.7	2.1	0.4	9.5	11.0	6.6	5.3	13.6	13.7	10.5	11.6
Er	2.3	4.4	2.4	2.8	3.7	3.2	5.7	1.9	0.5	11.3	12.4	7.8	5.5	16.6	15.5	11.8	13.5
Tm	2.3	3.8	2.3	1.8	3.3	2.2	3.7	1.0	0.4	9.6	9.8	6.5	2.9	13.4	13.3	8.2	10.1
Yb	4.0	5.5	3.6	2.5	4.7	2.9	6.1	1.6	0.7	13.6	14.0	9.6	4.1	19.9	19.6	11.6	14.5
Lu	4.4	6.1	4.2	1.9	4.8	3.0	6.3	1.7	0.7	14.	14.	10.	4.2	21.	22.	11.	15.

										7	0	2		4	3	9	4
La(n)/Yb(n)	11.7	6.6	6.5	136.8	7.6	38.8	64.1	53.8	59.9	19.9	14.4	17.0	130.6	20.0	15.4	42.8	28.7
Eu*	3.1	1.4	3.3	0.5	1.5	0.4	0.6	0.2	2.3	0.3	0.3	0.8	0.4	0.3	0.3	0.3	0.3
Ta+Yb	0.7	1.1	0.8	0.7	1.0	0.6	1.4	0.8	0.2	2.7	2.8	2.0	0.9	4.3	4.3	2.5	3.0

* LG: leucogranite; LS: leucosome

Table 3: Rare Earth Element compositions of Trivandrum Block Samples. (b) migmatites and restites

Sample	KLP-2	CKL-3	KAI-5	ASM-2	CKL-1	NEL-1	NEL-2	KAI-2	KAI-4	KNJ-2	KBL-2	NEL-4	ASM-1	CKL-2	KTP-1
Rock type	Mig*	Mig	Mig	Mig	Mig	Mig	Mig	Mig	Mig	Mig	Mig	Rest*	Rest	Rest	Rest
La	64	72	65	18	36	50	40	46	66	58	64	41	42	48	78
Ce	122	140	133	38	72	101	74	89	106	110	128	73	87	96	172
Pr	12.4	14.4	14.0	4.2	7.6	10.6	7.2	9.0	9.3	11.3	13.8	7.1	9.3	9.9	19.5
Nd	44.5	53.8	53.9	16.7	30.1	41.6	26.2	33.4	30.4	42.1	51.3	25.0	36.2	38.1	77.6
Sm	8.4	8.9	9.3	2.9	5.3	7.3	4.0	5.3	3.6	7.3	10.0	3.9	6.5	6.5	14.7
Eu	1.1	1.8	1.2	0.6	1.4	1.7	1.3	1.5	1.7	1.3	0.6	1.5	1.4	1.6	1.7
Gd	7.3	7.0	6.6	2.2	4.3	6.1	2.8	4.6	2.8	6.2	8.3	3.1	4.9	5.0	11.9
Tb	1.1	1.0	0.8	0.3	0.7	1.0	0.3	0.8	0.3	1.0	1.4	0.4	0.7	0.7	2.2
Dy	7.1	6.4	3.7	1.9	4.6	7.2	1.4	6.4	1.1	6.7	10.6	2.8	4.5	4.0	15.9
Ho	0.8	0.7	0.3	0.2	0.6	0.8	0.1	0.9	0.1	0.8	1.4	0.4	0.5	0.4	1.8
Er	2.6	2.5	1.0	0.8	2.0	2.8	0.5	3.7	0.4	2.7	5.6	1.3	1.9	1.4	5.8
Tm	0.3	0.3	0.1	0.1	0.3	0.4	0.1	0.5	0.0	0.4	0.8	0.2	0.2	0.2	0.7
Yb	3.5	3.3	1.1	0.9	2.8	3.7	0.6	5.9	0.5	3.7	9.1	2.0	2.5	1.6	6.2
Lu	0.6	0.6	0.2	0.2	0.5	0.6	0.1	1.1	0.1	0.6	1.5	0.3	0.4	0.3	0.8
chondrite normalised REE															
La	273.2	307.2	277.8	75.6	152.0	214.4	171.9	195.0	280.0	248.2	270.6	174.2	177.5	206.3	330.3
Ce	201.7	232.1	221.0	62.3	118.7	167.4	123.0	147.9	175.9	182.1	212.0	120.7	143.9	159.5	285.5
Pr	139.5	161.9	157.7	46.8	85.5	118.8	81.0	101.5	104.0	126.3	154.4	79.4	104.6	111.1	219.0
Nd	98.3	118.9	119.1	36.9	66.5	92.1	57.9	73.8	67.3	93.2	113.4	55.3	79.9	84.2	171.6
Sm	57.1	60.3	63.1	19.6	36.1	49.4	27.3	36.3	24.7	49.8	68.0	26.4	44.2	44.0	99.8
Eu	19.0	32.9	21.5	11.0	24.2	30.3	22.6	27.5	31.2	23.6	10.0	26.8	24.7	28.8	29.9
Gd	36.9	35.5	33.3	11.2	22.0	31.0	14.2	23.6	14.1	31.5	42.3	15.5	24.7	25.5	60.6
Tb	30.6	28.0	20.9	8.4	18.8	28.6	8.5	21.3	7.1	26.8	37.9	12.2	20.1	18.9	59.3
Dy	29.1	26.5	15.2	8.0	18.9	29.5	5.9	26.4	4.4	27.5	43.7	11.6	18.7	16.3	65.6
Ho	13.8	13.1	5.8	3.9	10.1	15.1	2.6	16.1	1.9	14.1	25.7	6.4	9.6	8.1	32.1
Er	16.6	15.9	6.2	4.7	12.9	17.5	3.0	23.0	2.3	16.9	35.3	8.3	11.7	8.8	36.6
Tm	14.0	13.6	4.5	3.9	11.2	14.9	2.4	22.1	1.9	14.6	33.3	7.3	10.1	6.8	27.9
Yb	21.3	20.1	7.0	5.6	17.4	22.5	3.8	36.3	2.8	22.6	55.8	12.0	15.6	9.7	37.9
Lu	24.1	23.1	8.2	6.2	18.6	25.9	4.5	43.4	3.7	24.2	63.1	13.8	17.0	10.5	34.2
La(n)/Yb(n)	12.8	15.2	39.6	13.6	8.7	9.5	45.3	5.4	100.0	11.0	4.8	14.5	11.4	21.2	8.7
Eu*	0.4	0.7	0.4	0.7	0.8	0.8	1.1	0.9	1.6	0.6	0.2	1.3	0.7	0.8	0.4
Ta+Yb	4.3	3.5	1.5	1.2	3.2	4.5	1.3	6.6	0.8	4.2	10.2	2.8	3.0	1.8	6.9

* Mig: migmatitic gneiss; Rest: restitic gneiss

Table 4: Zirconium Thermometry of Trivandrum Block leucogranites and leucosomes

Sample	Rock type	Cation Ratio	Zr (ppm)	$T_{(Zr)}$°C
KLP-1	leucogranite	1.12	62	728
KAI-3	leucogranite	1.23	9	591
KNJ-1	leucogranite	1.19	21	647
PLK-3	leucogranite	1.24	47	698
PLK-1	leucogranite	1.23	8	584
KBL-1	leucogranite	1.14	86	752
KLP-3	leucogranite	1.21	44	696
PLK-2	leucogranite	0.99	85	762
KNJ-3	leucogranite	1.25	4	544
MLK-3	leucogranite	1.37	67	717
KBL-3	leucogranite	1.05	197	832
KNN-2	leucogranite	1.24	31	670
KTP-2	leucogranite	1.37	71	722
MLK-1	leucosome	1.39	181	798
MLK-2	leucosome	1.34	157	789
KNN-1 A	leucosome	1.40	67	715
KNN-3	leucosome	1.22	62	721

$T_{(Zr)}$°C: Zr saturation temperature, Watson and Harrison (1983)

Table 5: Heat production estimates for Trivandrum Block leucogranites, leucosomes, migmatites and restites

Sample	Rock type	U+Th	K_2O	Calculated density (g/cm^3)	Present heat production ($\mu W/m^3$)	550 Ma heat production ($\mu W/m^3$)
KLP-1	leucogranite	6.46	5.53	2.71	1.09	1.25
KAI-3	leucogranite	0.83	4.70	2.71	0.52	0.63
KNJ-1	leucogranite	1.15	5.76	2.69	0.67	0.81
PLK-3	leucogranite	23.95	5.73	2.69	2.50	2.71
PLK-1	leucogranite	0.62	4.70	2.71	0.47	0.57
KBL-1	leucogranite	10.70	5.13	2.73	1.72	1.92
KLP-3	leucogranite	33.29	4.72	2.73	3.01	3.21
PLK-2	leucogranite	12.44	4.38	2.76	2.08	2.30
KNJ-3	leucogranite	3.59	5.85	2.70	0.91	1.06
MLK-3	leucogranite	10.18	6.58	2.73	2.71	3.05
KBL-3	leucogranite	19.77	5.36	2.79	2.73	2.99
KNN-2	leucogranite	9.36	6.54	2.75	1.62	1.83
KTP-2	leucogranite	37.18	5.11	2.74	3.20	3.41
MLK-1	leucosome	31.83	4.67	2.79	3.40	3.66
MLK-2	leucosome	20.69	4.05	2.81	2.20	2.38
KNN-1 A	leucosome	49.75	5.60	2.77	4.50	4.78
KNN-3	leucosome	38.28	4.71	2.81	3.70	3.95
KLP-2	migmatite	12.68	3.25	2.90	1.77	1.93
CKL-3	migmatite	8.60	3.26	2.86	1.02	1.13
KAI-5	migmatite	17.64	2.66	2.86	1.67	1.78
ASM-2	migmatite	4.23	3.30	2.86	0.65	0.74
CKL-1	migmatite	3.27	2.27	2.93	0.52	0.58
NEL-1	migmatite	7.44	3.29	2.92	1.01	1.13
NEL-2	migmatite	1.43	1.64	2.94	0.34	0.39
KAI-2	migmatite	3.19	2.90	2.99	0.59	0.68
KAI-4	migmatite	9.67	1.93	2.91	0.94	1.01
KNJ-2	migmatite	10.92	3.53	2.99	1.48	1.62
KBL-2	migmatite	18.25	2.19	3.00	2.13	2.28
NEL-4	restite	5.75	4.37	2.96	1.02	1.16
ASM-1	restite	10.09	1.51	2.95	1.13	1.22
CKL-2	restite	8.04	3.07	3.03	1.12	1.23
KTP-1	restite	5.60	4.66	3.00	1.13	1.29

***** HP = (density/100)*[(9.5122*U)+(2.56*Th)+(3.54*K)] where density is in gcm^{-3}, U and Th in ppm, K in wt% element

** ^{238}U, ^{235}U, ^{232}Th and ^{40}K at 550 Ma are calculated from present day U, Th and K using appropriate decay equations for each isotope

Highlights:

- Leucogranite and leucosome geochemical variations in high-grade migmatites are controlled by peritectic phase assemblage entrainment, complemented by near-source feldspar-controlled crystal fractionation and crystal accumulation accompanied by loss of fractionated melt.
- Cumulate leucogranites are characterised by highly positive Eu* at low total HREE, and low HFSE. Their extremely low Zr that result in anomalous zirconium saturation temperatures.
- Crustal heat production in the Trivandrum Block at 20-30 km depths and 550 Ma is estimated to have been 2.0 ± 0.6 μWm^{-3}. Although elevated, this is not high enough to of itself generate the near-UHT to UHT metamorphism in this orogen.

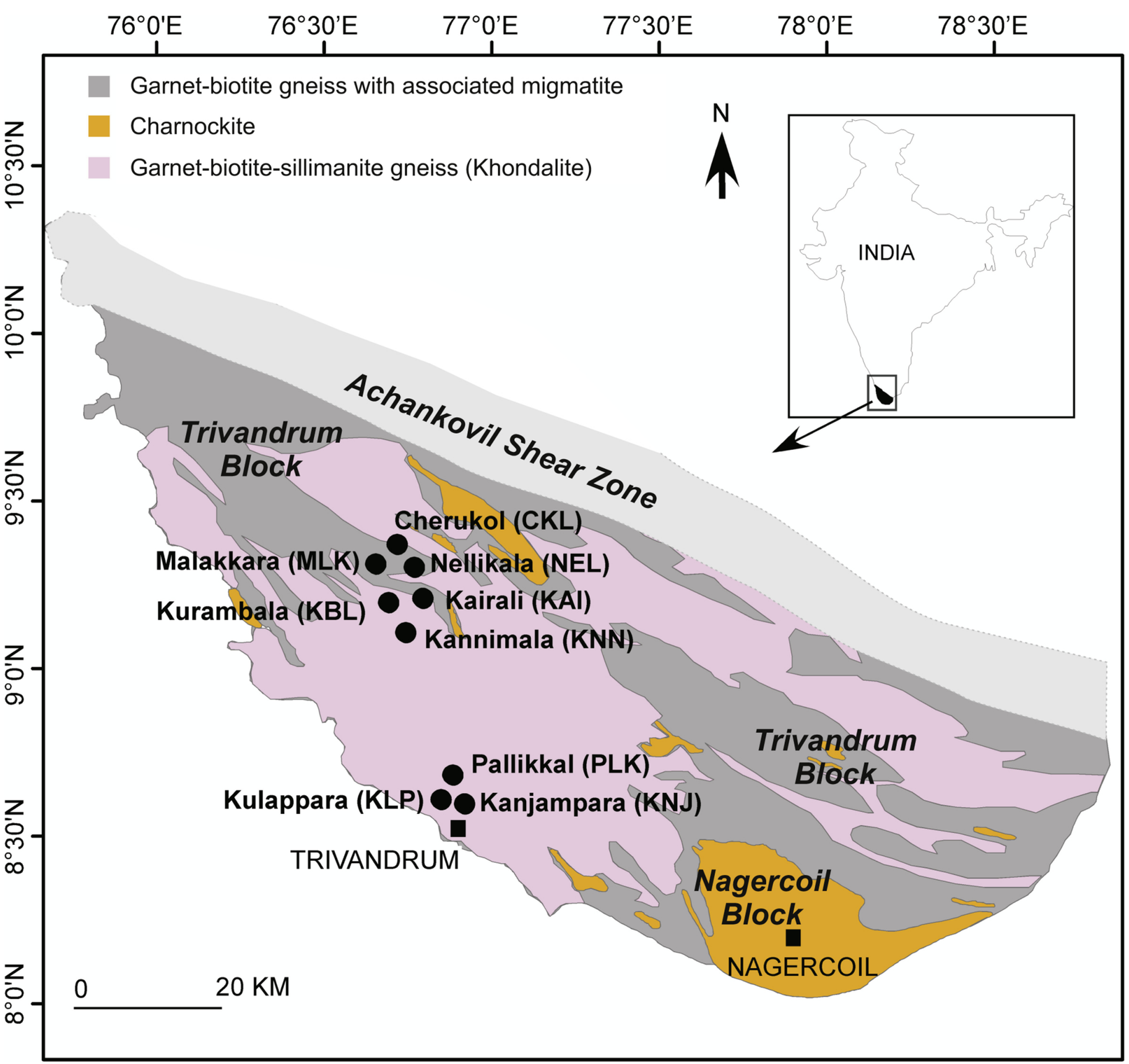
76°0'E
76°30'E
77°0'E
77°30'E
78°0'E
78°30'E
10°30'N
10°0'N
9°30'N
9°0'N
8°30'N
8°0'N
Garnet-biotite gneiss with associated migmatite
Charnockite
Garnet-biotite-sillimanite gneiss (Khondalite)
N
INDIA
Achankovil Shear Zone
Trivandrum Block
Cherukol (CKL)
Malakkara (MLK)
Nellikala (NEL)
Kurambala (KBL)
Kairali (KAI)
Kannimala (KNN)
Pallikkal (PLK)
Kulappara (KLP)
Kanjampara (KNJ)
TRIVANDRUM
Trivandrum Block
Nagercoil Block
NAGERCOIL
0
20 KM

Figure 1

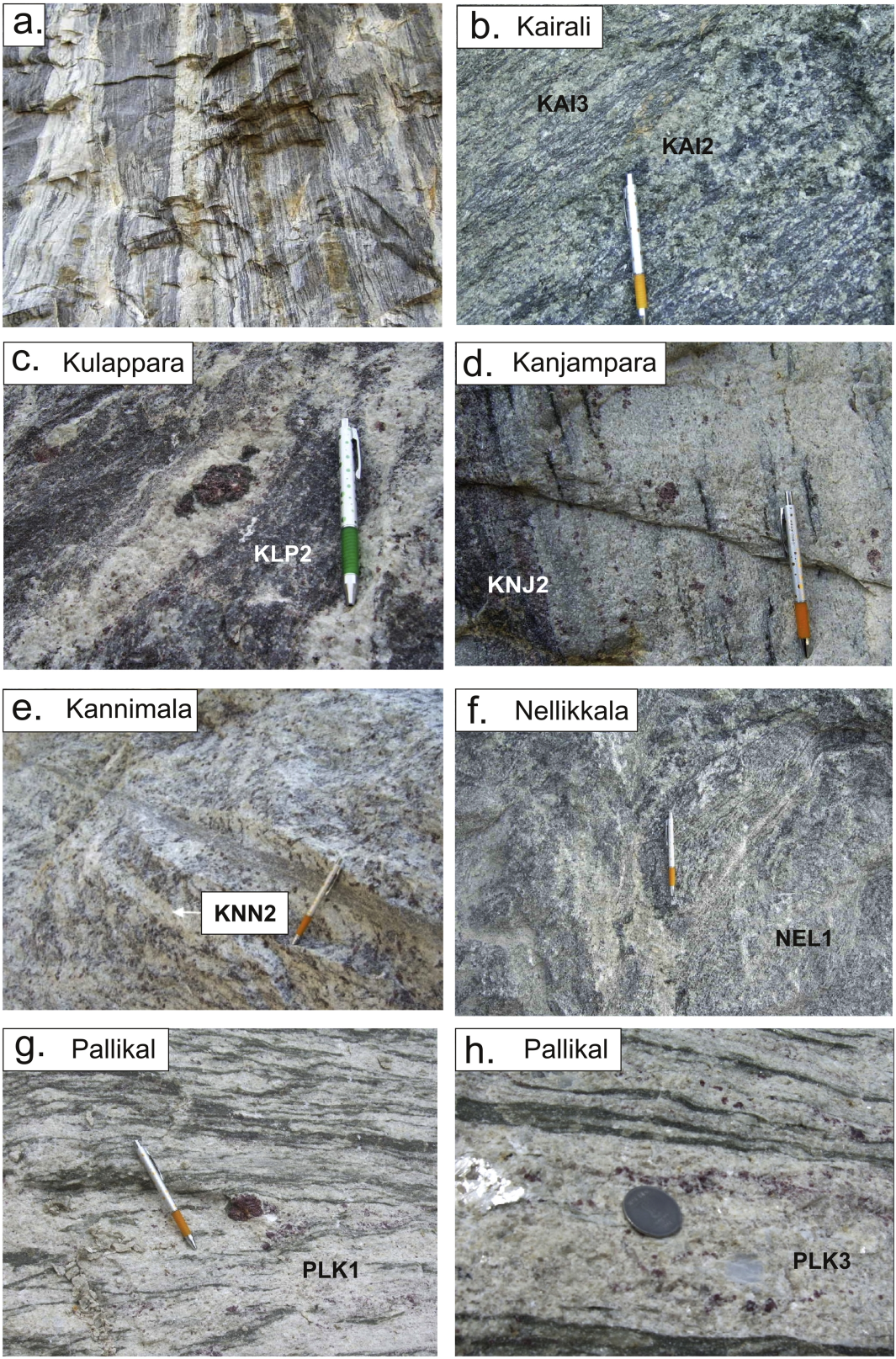
a.
b. Kairali
KAI3
KAI2
c. Kulappara
KLP2
d. Kanjampara
KNJ2
e. Kannimala
KNN2
f. Nellikkala
NEL1
g. Pallikal
PLK1
h. Pallikal
PLK3

Figure 2

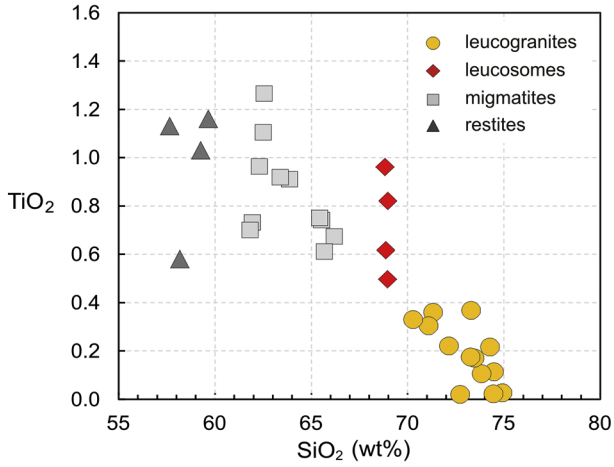
leucogranites
leucosomes
migmatites
restites
TiO2
SiO2 (wt%)

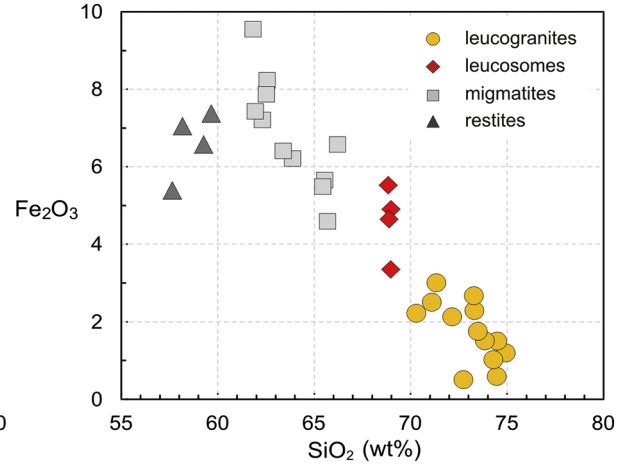
leucogranites
leucosomes
migmatites
restites
Fe2O3
SiO2 (wt%)

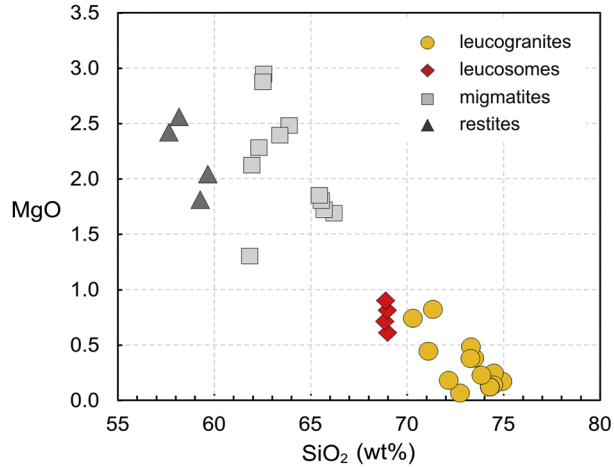
leucogranites
leucosomes
migmatites
restites
MgO
SiO2 (wt%)

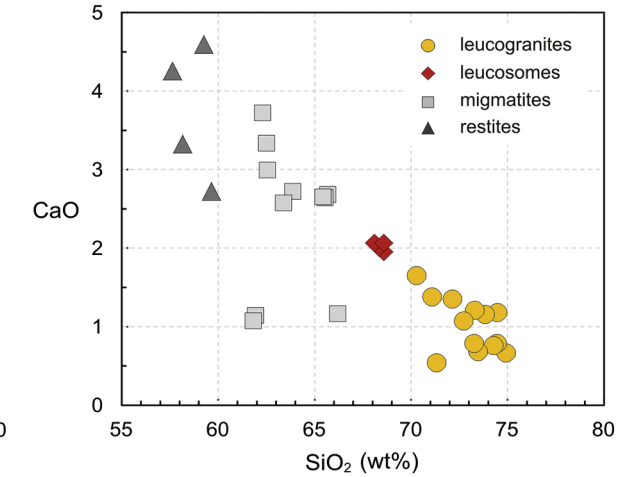
leucogranites
leucosomes
migmatites
restites
CaO
SiO2 (wt%)

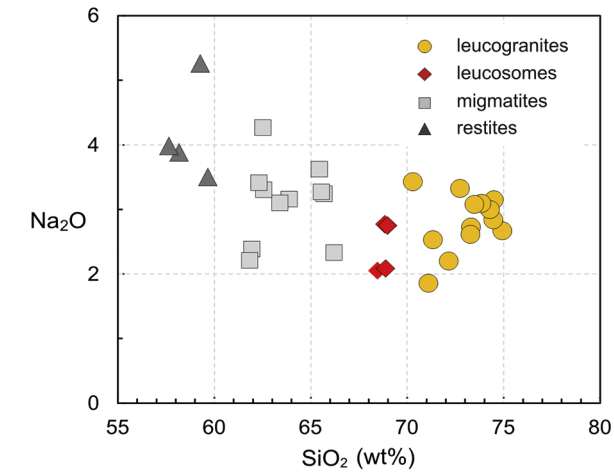
leucogranites
leucosomes
migmatites
restites
Na2O
SiO2 (wt%)

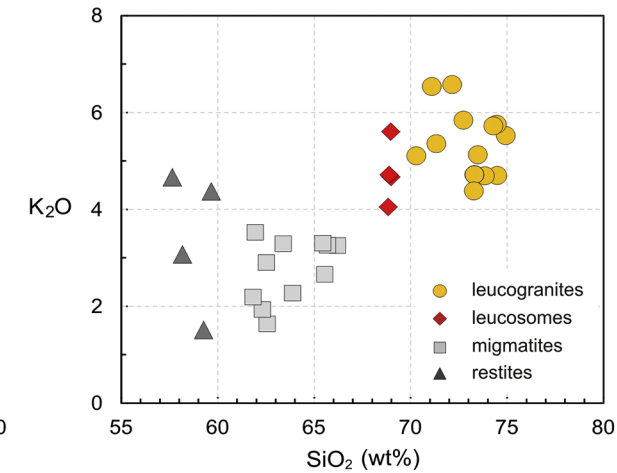
leucogranites
leucosomes
migmatites
restites
K2O
SiO2 (wt%)

Figure 3

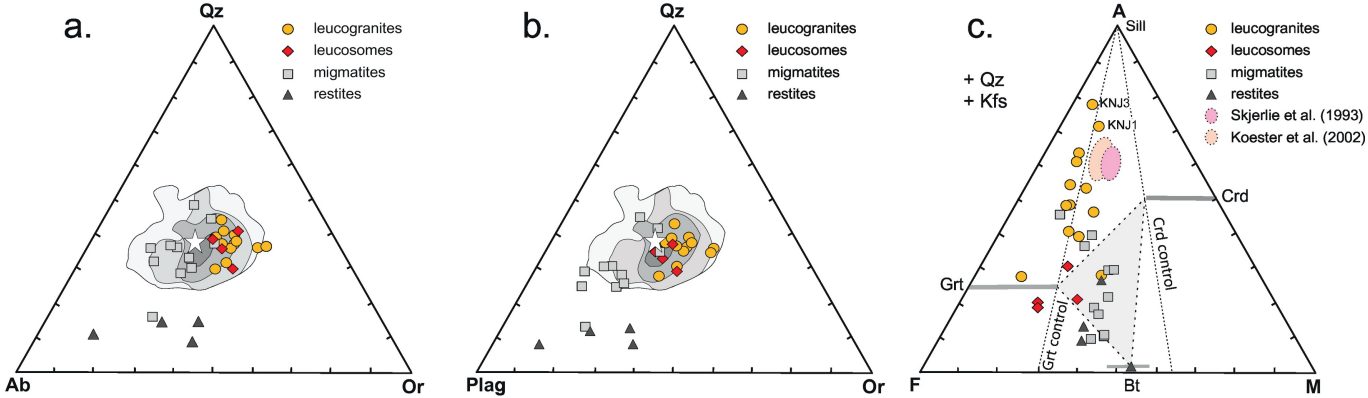
a.
Qz
Ab
Or
leucogranites
leucosomes
migmatites
restites
b.
Qz
Plag
Or
leucogranites
leucosomes
migmatites
restites
c.
A
Sill
+ Qz
+ Kfs
KNJ3
KNJ1
Crd
Crd control
Grt
Grt control
F
Bt
M
leucogranites
leucosomes
migmatites
restites
Skjerlie et al. (1993)
Koester et al. (2002)

Figure 4

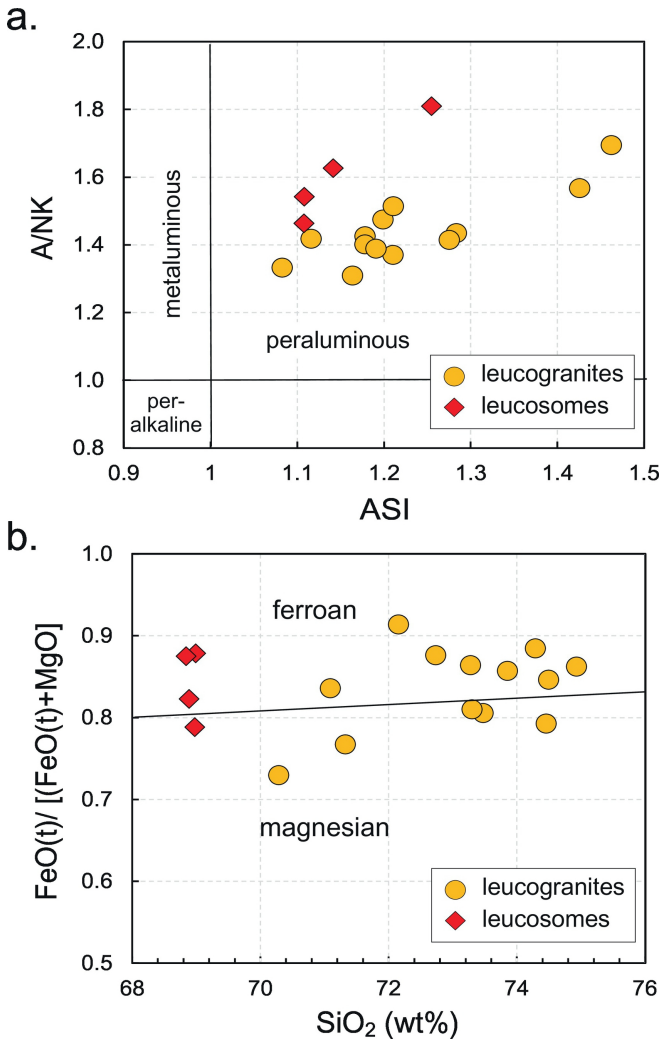
a.
2.0
1.8
1.6
1.4
1.2
1.0
0.8
A/NK
metaluminous
peraluminous
per-
alkaline
leucogranites
leucosomes
0.9
1
1.1
1.2
1.3
1.4
1.5
ASI
b.
1.0
0.9
0.8
0.7
0.6
0.5
FeO(t)/ [(FeO(t)+MgO]
ferroan
magnesian
leucogranites
leucosomes
68
70
72
74
76
SiO2 (wt%)

Figure 5

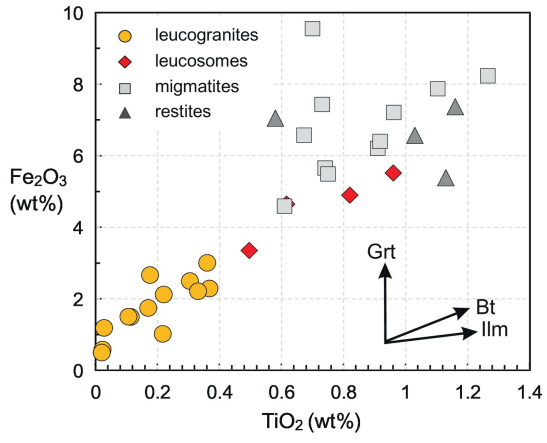
leucogranites
leucosomes
migmatites
restites
Fe2O3 (wt%)
TiO2 (wt%)
Grt
Bt
Ilm

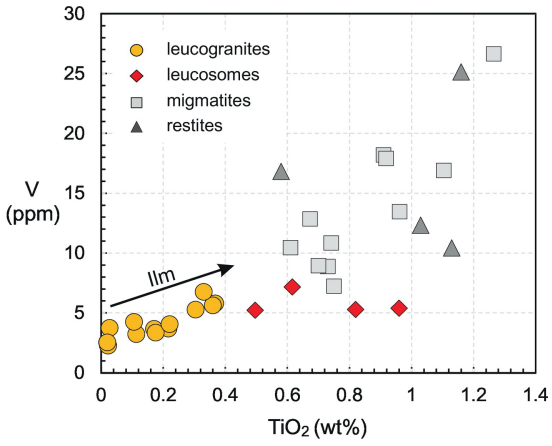
leucogranites
leucosomes
migmatites
restites
V (ppm)
TiO2 (wt%)
Ilm

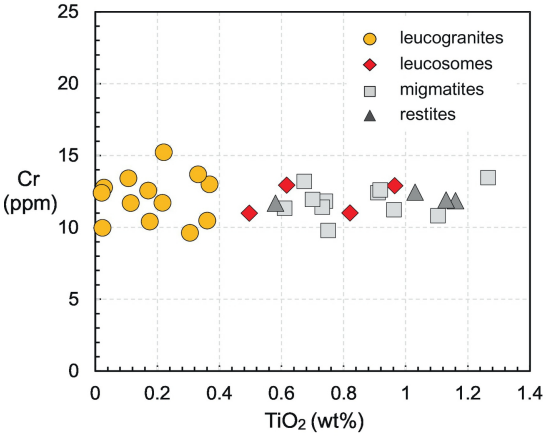
leucogranites
leucosomes
migmatites
restites
Cr (ppm)
TiO2 (wt%)

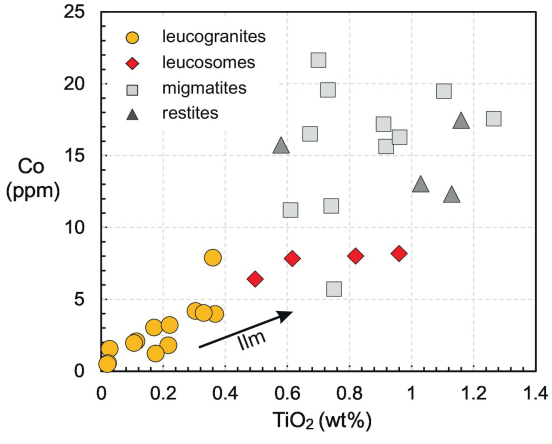
leucogranites
leucosomes
migmatites
restites
Co (ppm)
TiO2 (wt%)
Ilm

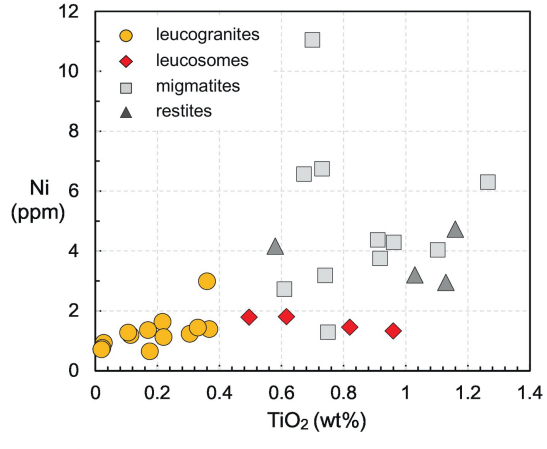
leucogranites
leucosomes
migmatites
restites
Ni (ppm)
TiO2 (wt%)

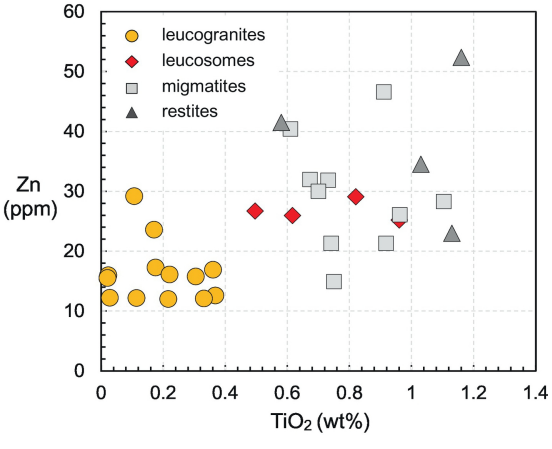
leucogranites
leucosomes
migmatites
restites
Zn (ppm)
TiO2 (wt%)

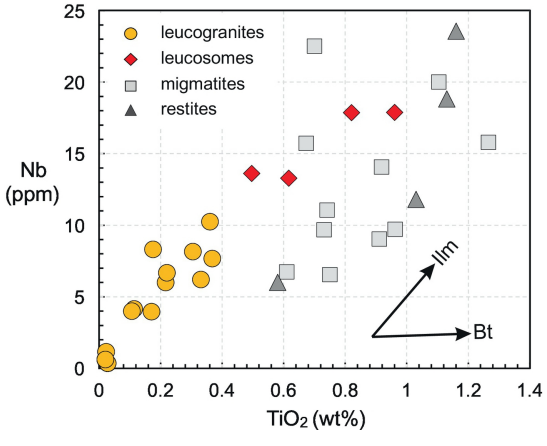
leucogranites
leucosomes
migmatites
restites
Nb (ppm)
TiO2 (wt%)
Ilm
Bt

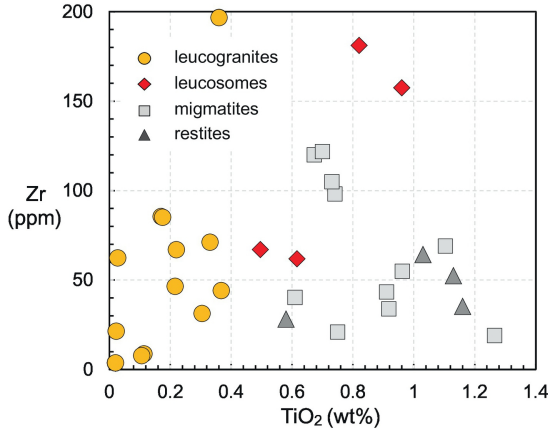
leucogranites
leucosomes
migmatites
restites
Zr (ppm)
TiO2 (wt%)

Figure 6

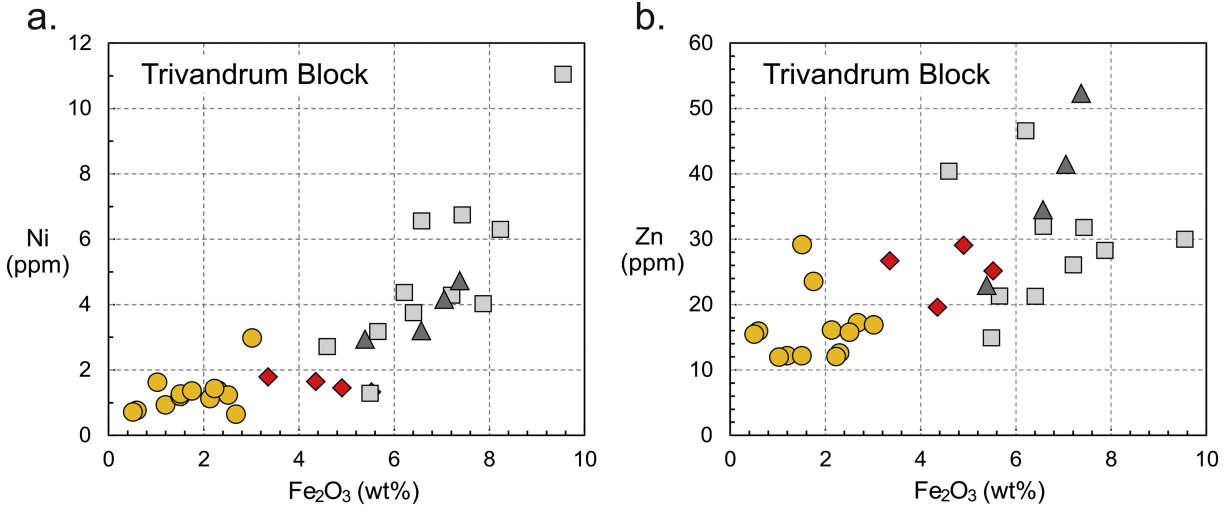
a.
Trivandrum Block
Ni (ppm)
Fe2O3 (wt%)
0
2
4
6
8
10
12
b.
Trivandrum Block
Zn (ppm)
Fe2O3 (wt%)
0
10
20
30
40
50
60

Figure 7

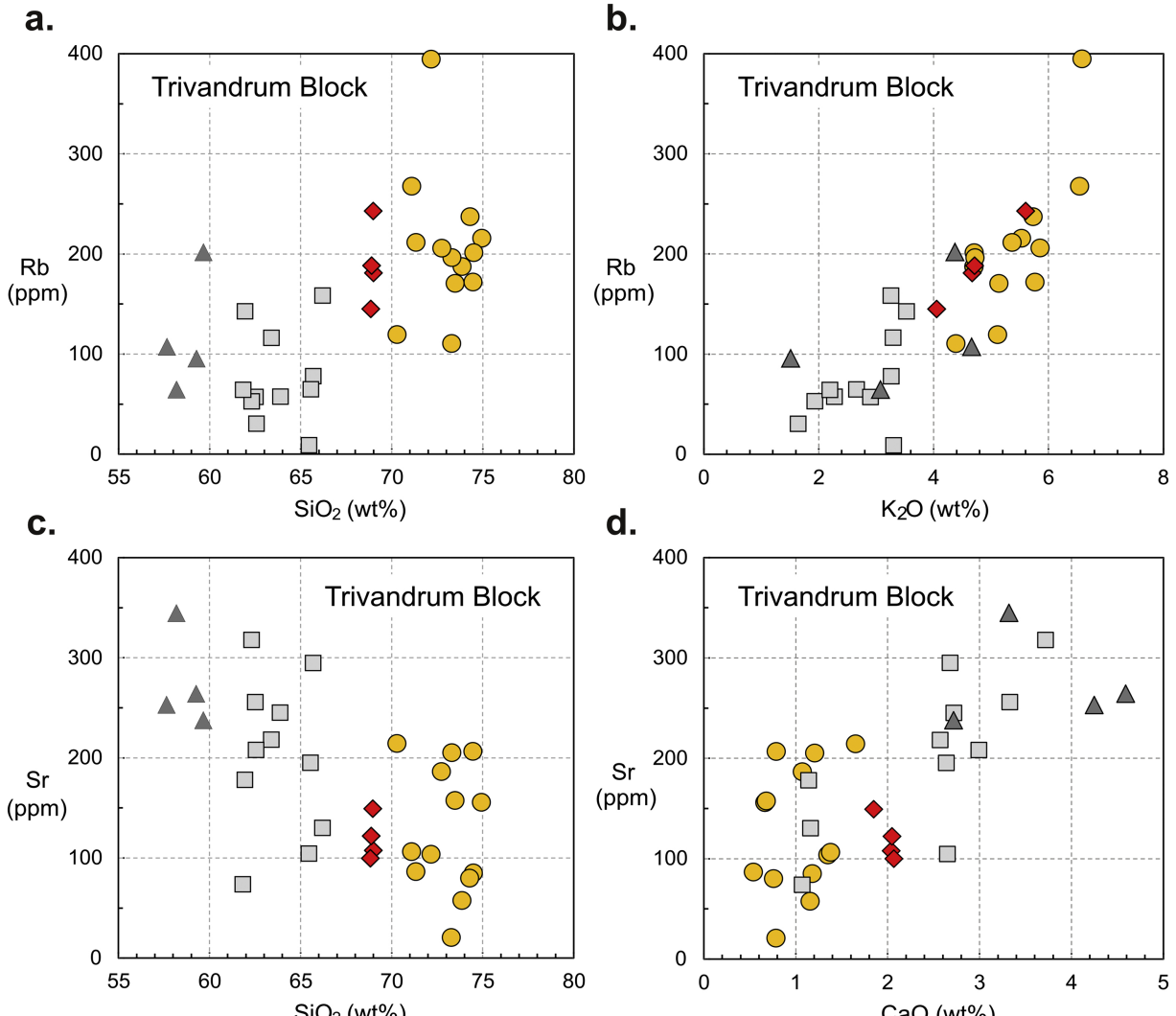
a.
Trivandrum Block
Rb (ppm)
SiO2 (wt%)
b.
Trivandrum Block
Rb (ppm)
K2O (wt%)
c.
Trivandrum Block
Sr (ppm)
SiO2 (wt%)
d.
Trivandrum Block
Sr (ppm)
CaO (wt%)

Figure 8

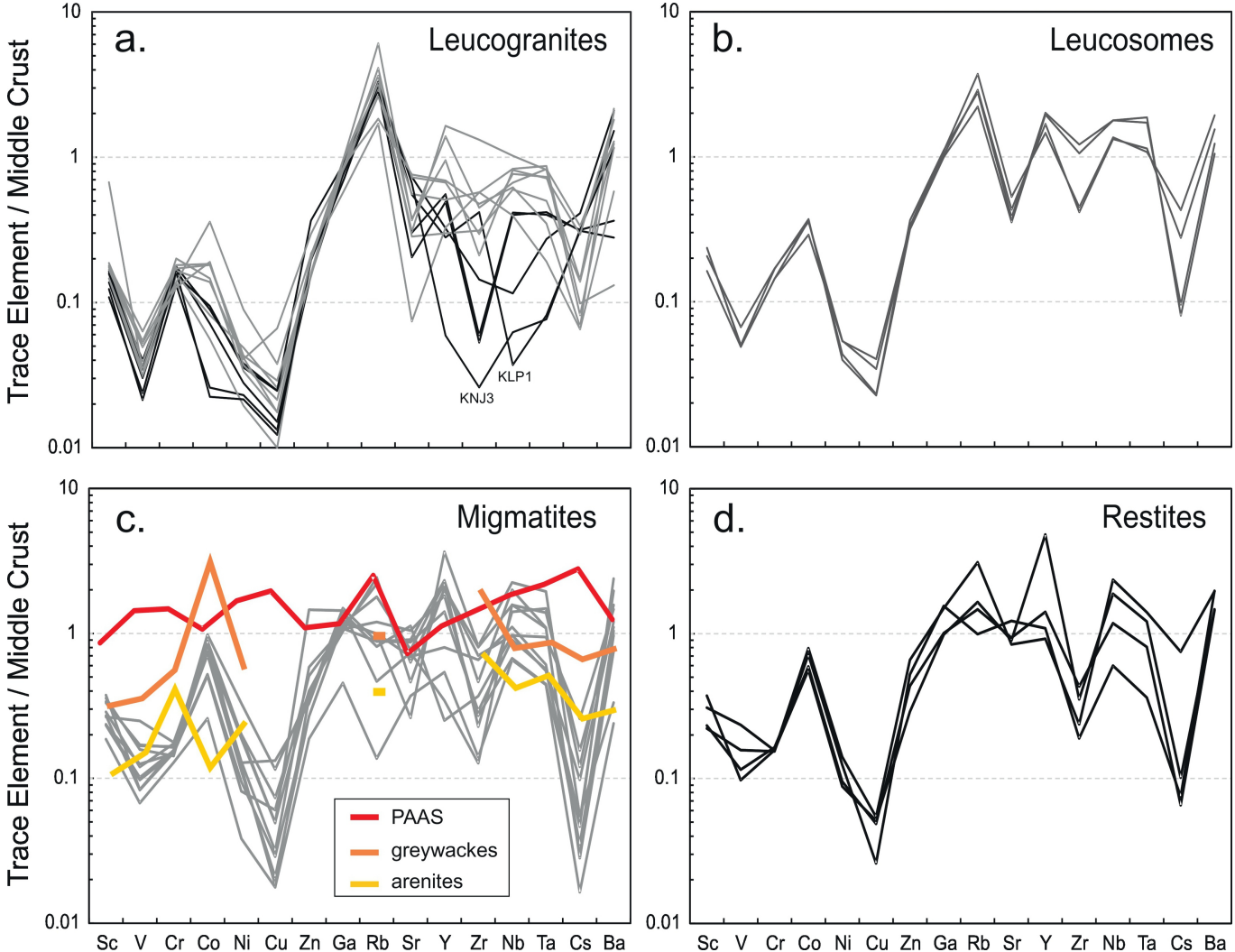
a.
Leucogranites
b.
Leucosomes
c.
Migmatites
d.
Restites
Trace Element / Middle Crust
10
1
0.1
0.01
KLP1
KNJ3
PAAS
greywackes
arenites
Sc V Cr Co Ni Cu Zn Ga Rb Sr Y Zr Nb Ta Cs Ba

Figure 9

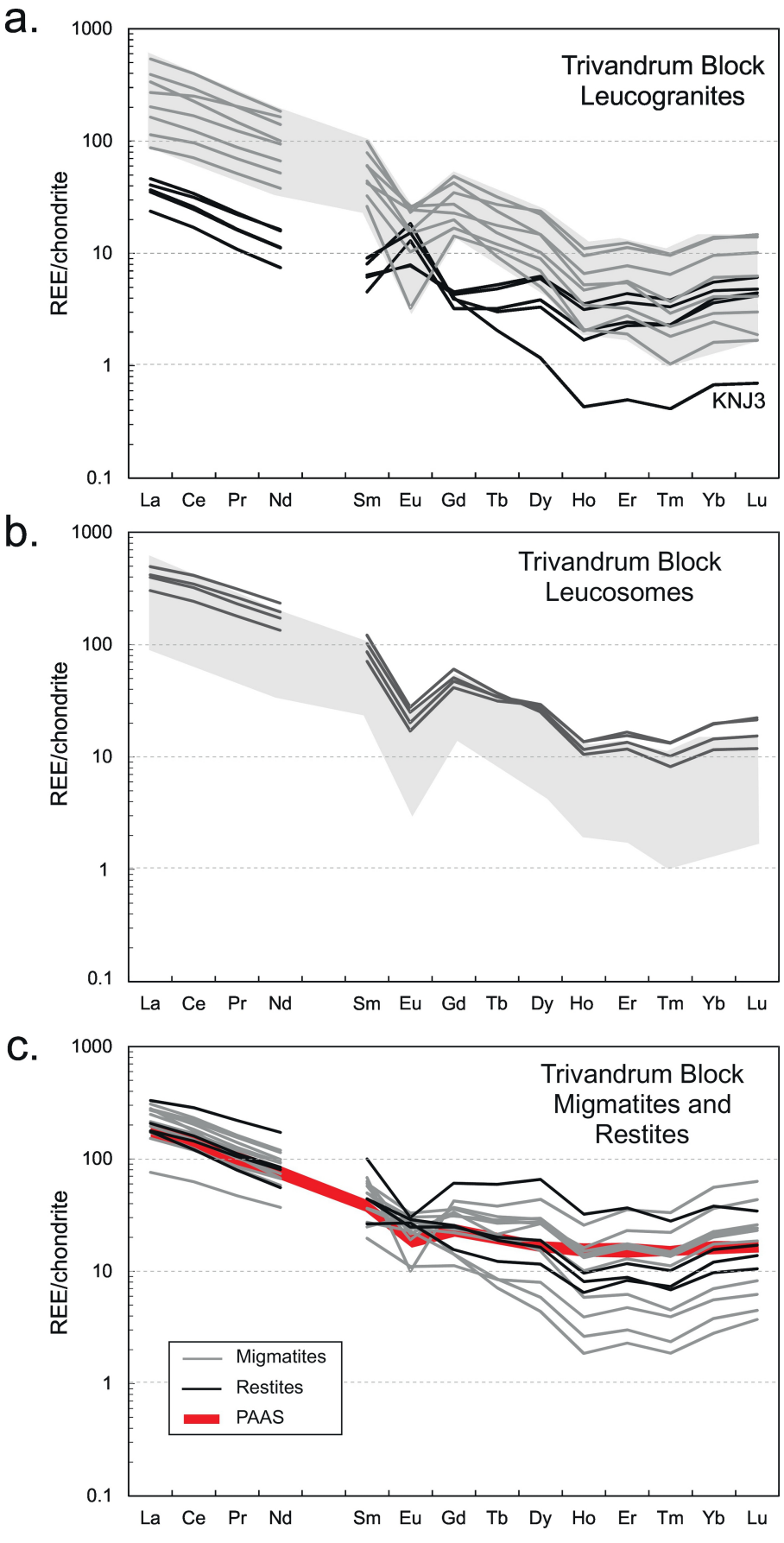
a.
Trivandrum Block
Leucogranites
KNJ3
b.
Trivandrum Block
Leucosomes
c.
Trivandrum Block
Migmatites and
Restites
Migmatites
Restites
PAAS
REE/chondrite
1000
100
10
1
0.1
La Ce Pr Nd Sm Eu Gd Tb Dy Ho Er Tm Yb Lu

Figure 10

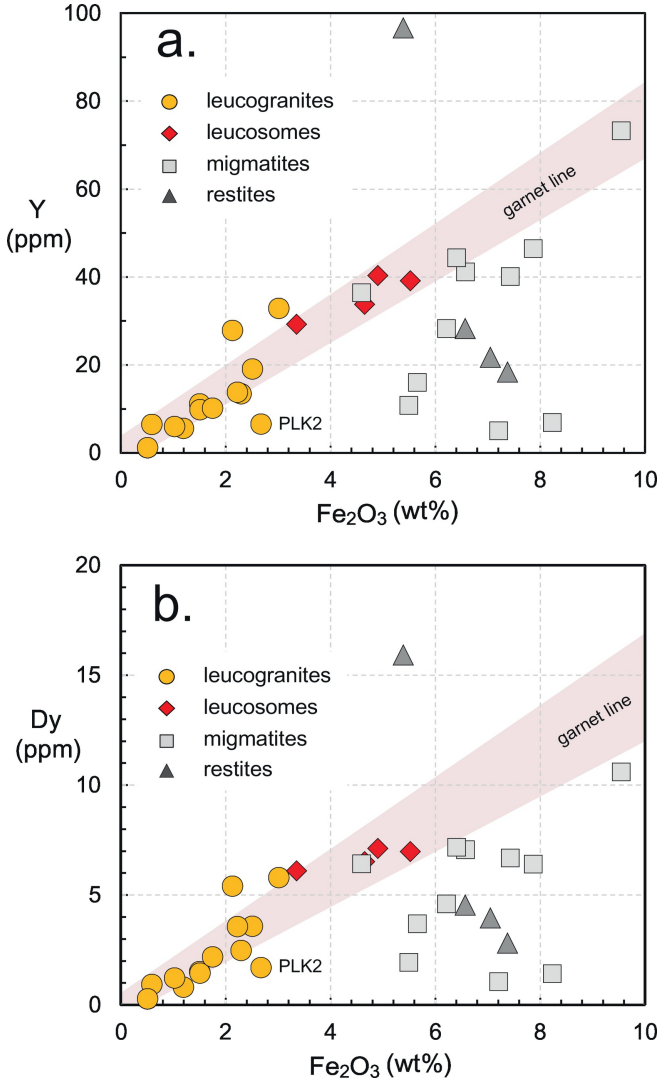
a.
leucogranites
leucosomes
migmatites
restites
garnet line
PLK2
Y (ppm)
Fe2O3 (wt%)
b.
leucogranites
leucosomes
migmatites
restites
garnet line
PLK2
Dy (ppm)
Fe2O3 (wt%)

Figure 11

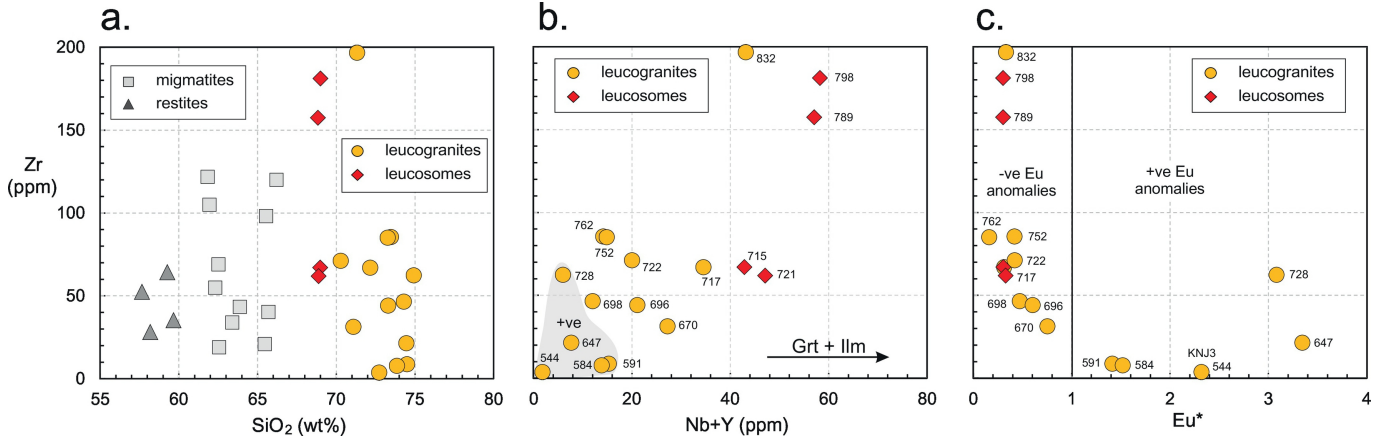
a.
migmatites
restites
leucogranites
leucosomes
Zr (ppm)
SiO2 (wt%)
b.
leucogranites
leucosomes
+ve
Grt + Ilm
Nb+Y (ppm)
c.
leucogranites
leucosomes
-ve Eu anomalies
+ve Eu anomalies
KNJ3
Eu*

Figure 12

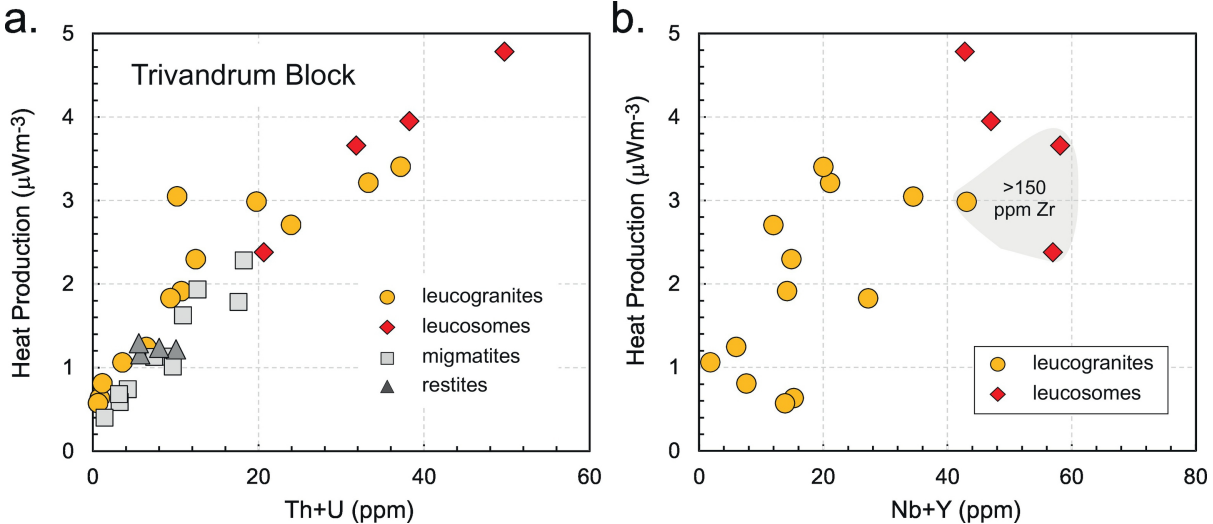
a.
Trivandrum Block
Heat Production (μWm-3)
Th+U (ppm)
leucogranites
leucosomes
migmatites
restites
b.
Heat Production (μWm-3)
Nb+Y (ppm)
>150
ppm Zr
leucogranites
leucosomes

Figure 13

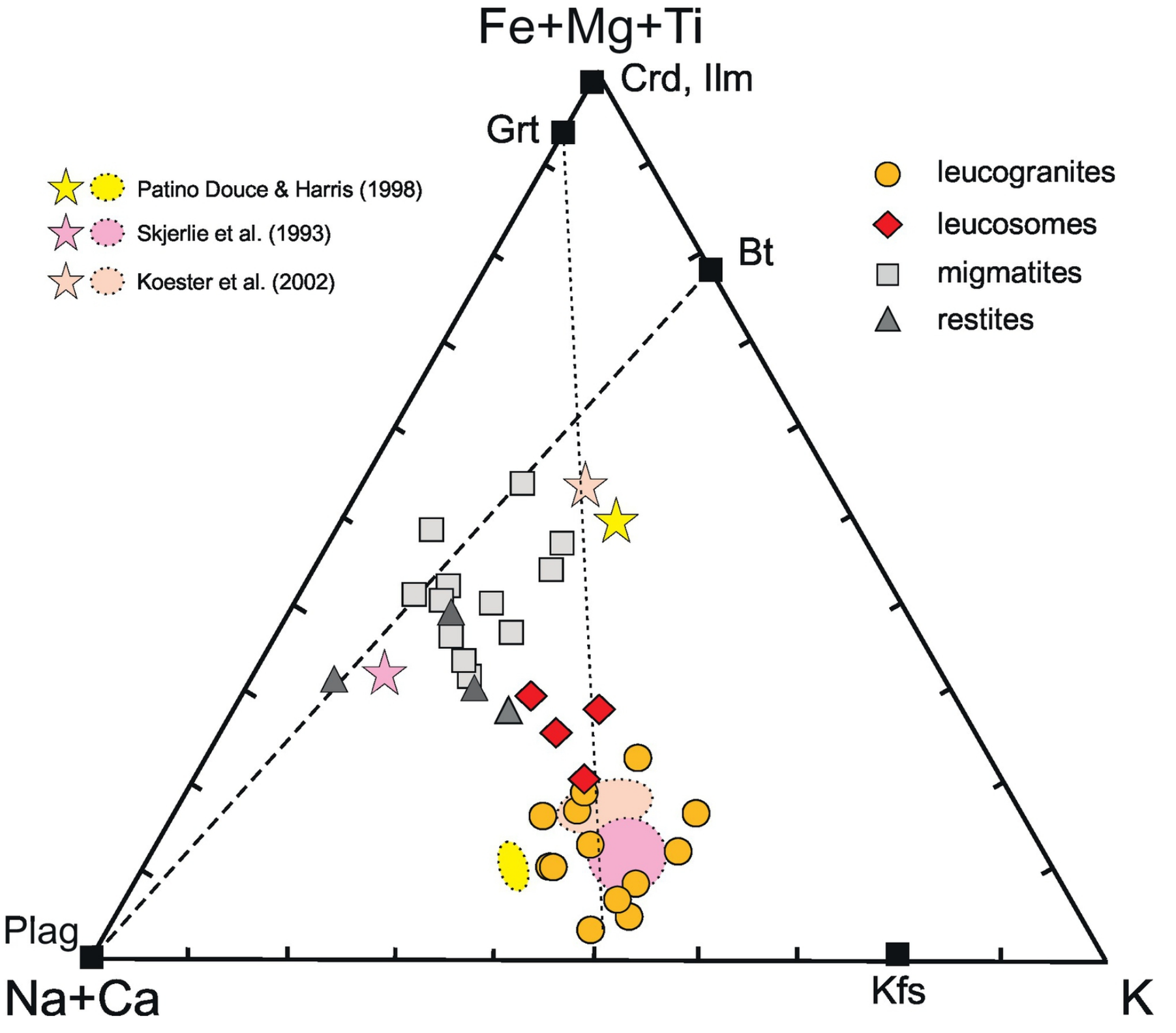
Fe+Mg+Ti
Crd, Ilm
Grt
Bt
Plag
Na+Ca
Kfs
K
Patino Douce & Harris (1998)
Skjerlie et al. (1993)
Koester et al. (2002)
leucogranites
leucosomes
migmatites
restites

Figure 14

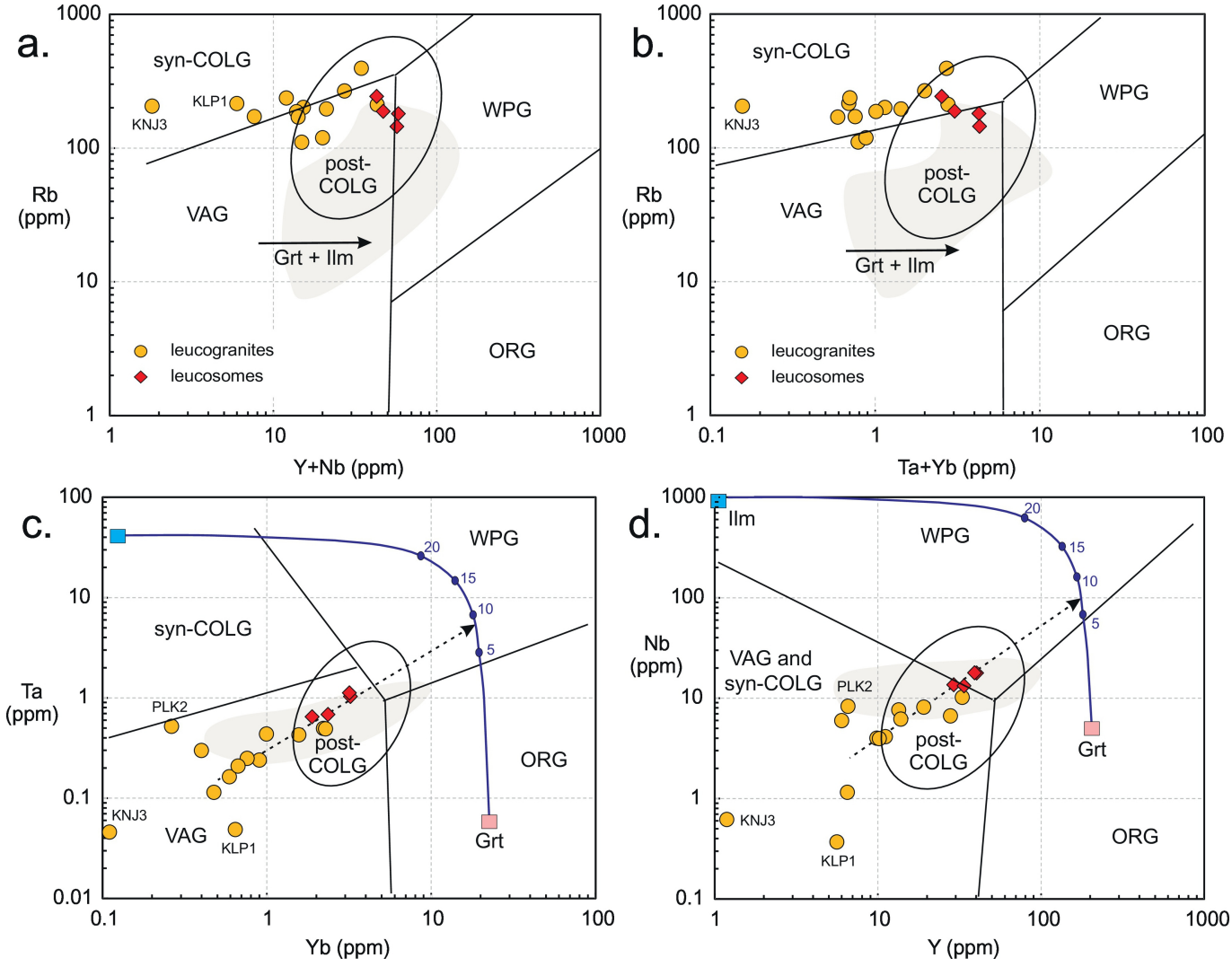
a.
syn-COLG
KLP1
KNJ3
WPG
post-
COLG
VAG
Grt + Ilm
leucogranites
leucosomes
ORG
Rb
(ppm)
Y+Nb (ppm)
b.
syn-COLG
KNJ3
WPG
post-
COLG
VAG
Grt + Ilm
leucogranites
leucosomes
ORG
Rb
(ppm)
Ta+Yb (ppm)
c.
WPG
20
15
10
5
syn-COLG
PLK2
post-
COLG
ORG
KNJ3
VAG
KLP1
Grt
Ta
(ppm)
Yb (ppm)
d.
Ilm
WPG
20
15
10
5
VAG and
syn-COLG
PLK2
post-
COLG
Grt
KNJ3
KLP1
ORG
Nb
(ppm)
Y (ppm)

Figure 15

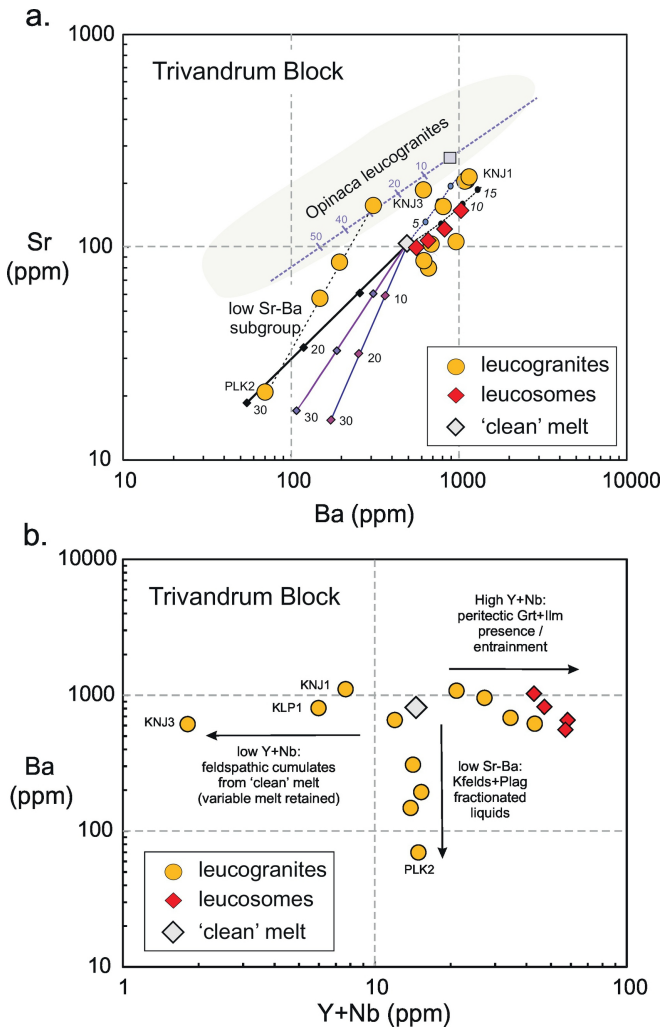
a.
Trivandrum Block
Opinaca leucogranites
low Sr-Ba subgroup
KNJ1
KNJ3
PLK2
leucogranites
leucosomes
'clean' melt
Sr (ppm)
Ba (ppm)
b.
Trivandrum Block
High Y+Nb: peritectic Grt+Ilm presence / entrainment
low Y+Nb: feldspathic cumulates from 'clean' melt (variable melt retained)
low Sr-Ba: Kfelds+Plag fractionated liquids
KNJ1
KLP1
KNJ3
PLK2
leucogranites
leucosomes
'clean' melt
Ba (ppm)
Y+Nb (ppm)

Figure 16